

Gamma-Ray Flash in the Interaction of a Tightly Focused Single-Cycle Ultraintense Laser Pulse with a Solid Target

P. Hadjisolomou^{1†}, T. M. Jeong¹, P. Valenta^{1,2}, D. Kolenaty¹, R. Versaci¹, V. Olšovcová¹, C. P. Ridgers³, and S. V. Bulanov^{1,4}

¹ELI Beamlines Centre, Institute of Physics, Czech Academy of Sciences, Za Radnicí 835, 25241 Dolní Břežany, Czech Republic

²Faculty of Nuclear Sciences and Physical Engineering, Czech Technical University in Prague, Břehova 7, Prague 11519, Czech Republic

³York Plasma Institute, Department of Physics, University of York, Heslington, York, North Yorkshire YO10 5DD, UK

⁴National Institutes for Quantum and Radiological Science and Technology (QST), Kansai Photon Science Institute, 8-1-7 Umemidai, Kizugawa, Kyoto 619-0215, Japan

(Received xx; revised xx; accepted xx)

We employ the λ^3 regime where a near-single-cycle laser pulse is tightly focused, thus providing the highest possible intensity for the minimal energy at a certain laser power. The quantum electrodynamics processes in the course of the interaction of the ultraintense laser with a solid target are studied via three-dimensional particle-in-cell simulations, revealing the generation of copious γ -photons and electron-positron pairs. The parametric study on the laser polarisation, target thickness and electron number density shows that the radially polarised laser provides the optimal regime for γ -photon generation. By varying the laser power in the range of 1 to 300 petawatt we find the scaling of the laser to γ -photon energy conversion efficiency. The laser-generated γ -photon interaction with a high-Z target is further studied by using Monte Carlo simulations revealing further electron-positron pair generation and radioactive nuclides creation.

1. Introduction

The invention of the Chirped Pulse Amplification (CPA) technique (Strickland & Mourou 1985) in mid-80's allowed the rapid growth of the laser power beyond the terawatt (TW) level. The petawatt (PW) threshold was exceeded at the end of 20th century (Perry *et al.* 1999). Currently, the record power is for the ELI-NP 10 PW laser (Tanaka *et al.* 2020), with another 10 PW laser near completion in ELI-Beamlines. Current worldwide activities on PW laser systems and further envisions to attain >100 PW lasers are summarized in (Danson *et al.* 2019; Li *et al.* 2021).

Since the laser power increases by either increasing the energy or reducing the pulse duration, a single-cycle pulse was proposed (Mourou *et al.* 2002; Bulanov *et al.* 2006; Voronin, A. A. and Zheltikov, A. M. and Ditmire, T. and Rus, B. and Korn, G. 2013). Post-compression of the CPA systems leads to near-single-cycle pulses by self-phase modulation in hollow-core fibres, although the energy is in the millijoule level (Böhle *et al.* 2014; Ouillé *et al.* 2020). A second technique producing near-single-cycle pulses is the Optical Parametric CPA, by which a 4.5 fs, 16 TW pulse is reported (Rivas *et al.* 2017). Reducing the pulse duration is the primary goal of ELI-ALPS,

† Email address for correspondence: Prokopis.Hadjisolomou@eli-beams.eu

where a 17 fs, 2 PW laser is under development (Osvay *et al.* 2019). Thus, at a given laser power, reduction of the pulse duration leads to a linear reduction of the energy, consequently the minimum laser energy for a single-cycle pulse.

However, it is most desired to reach the highest laser intensity rather than power. The quadratic dependency of the intensity on the inverse of the focal spot radius points on emphasizing for a reduced focal spot. More than two decades ago, a theoretical estimation of the minimum focal spot diameter (Sales 1998) suggests a value of $4\pi^{-2}\lambda$, where λ is the laser wavelength. A vectorial diffraction approach was adopted (Richards *et al.* 1959; April & Piché 2010) to describe a focal spot smaller than the wavelength. The benefit of the vectorial representation is that Maxwell's equations are satisfied at any point in space, and analytical expressions for the electric and magnetic field components can be calculated (April & Piché 2010; Salamin 2015; Jeong *et al.* 2015). Experimental implementation of the tight-focusing scheme by a parabola with f-number, f_N , (the ratio of the focal length, f , to the beam diameter, D) of 0.6 claims focusing of a 45 TW laser to a $\sim 0.8 \mu\text{m}$ focal spot diameter, leading to an intensity of $\sim 10^{22} \text{ Wcm}^{-2}$ (Bahk *et al.* 2004), where a similar intensity is achieved by focusing a 0.3 PW using a parabola of $f_N = 1.3$ (Pirozhkov *et al.* 2017).

Apart from the usually employed linearly polarised (LP) lasers, the radially polarised (RP) and azimuthally polarised (AP) lasers draw much interest of several research groups, employing multi-PW lasers for electron (Salamin 2010*a*; Payeur *et al.* 2012) and proton/ion (Salamin 2010*a*; Li *et al.* 2012; Ghotra & Kant 2015) acceleration. Let us define the laser propagation direction to be along \hat{x} . In cylindrical coordinates, a RP plane wave satisfies $E_r\hat{r} = cB_\phi\hat{\phi}$ everywhere, where $E_r\hat{r}$ is the radial electric field component, $B_\phi\hat{\phi}$ is the azimuthal magnetic field component and c is the speed of light in vacuum. For the AP laser, the electric and magnetic field components are interchanged. However, under tight-focusing conditions the relation $E_r\hat{r} = cB_\phi\hat{\phi}$ breaks down due to the appearance of a longitudinal electric field component, $E_x\hat{x}$ for a RP laser, and a longitudinal magnetic field component, $B_x\hat{x}$, for the AP laser (Salamin 2006, 2010*b*; Jeong *et al.* 2018). Compared to LP lasers, both RP and AP lasers were found experimentally to give a smaller focal spot (Dorn *et al.* 2003; Cheng *et al.* 2015), in agreement with the elongated electric field distribution for a LP laser (Jeong *et al.* 2018).

When the concept of a single-cycle laser is combined with the tight-focusing technique then the λ^3 regime is obtained, where for a certain laser power one can use minimal energy to achieve the highest intensity (Mourou *et al.* 2002). If the λ^3 regime is applied to an 100 PW laser, then an intensity exceeding 10^{25} Wcm^{-2} will be achieved. This ultra-intense regime is capable of providing a plethora of particles, such as γ -photons, leptons [electrons (e^-) and positrons (e^+)] and hadrons [protons (p^+) and/or heavy ions (i^+)] (Mourou *et al.* 2006). Although γ -photons are achievable even by near-PW class lasers, high laser to γ -photon energy conversion efficiency, κ_γ , is important for applications in photonuclear reactions (Nedorezov *et al.* 2004), astrophysical studies (Rees & Mészáros 1992; Bulanov *et al.* 2015; Philippov & Spitkovsky 2018; Aharonian *et al.* 2021) and study of the extremely high energy density on materials science (Eliasson & Liu 2013).

At laser intensities of $\sim 10^{24} \text{ Wcm}^{-2}$ the multiphoton Compton scattering process dominates the γ -photon emission (Ridgers *et al.* 2013; Lezhnin *et al.* 2018). During that process, a hot electron/positron is scattered after collision with the incident laser field, its velocity and direction values change and a scattered γ -photon is produced. The process is synopsised in $e^\pm + N\omega_l \rightarrow e^\pm + \omega_\gamma$ where ω_l is the central laser frequency, ω_γ is the scattered γ -photon frequency and $N \gg 1$ is the number of laser photons lost.

The Schwinger field represents the field required for the vacuum to break into an e^-e^+ pair, and it equals $E_S = m_e^2 c^3 / (e\hbar) \approx 1.3 \times 10^{18} \text{ Vm}^{-1}$, where m_e is the electron rest mass, \hbar is the reduced Planck constant and e is the elementary charge (Berestetskii *et al.* 1982). The probability that a γ -photon will be emitted through multiphoton Compton scattering depends on the parameter (Ritus 1970)

$$\chi_e = \sqrt{\left(\gamma_e \frac{\mathbf{E}}{E_S} + \frac{\mathbf{p}}{m_e} \times \frac{\mathbf{B}}{E_S}\right)^2 - \left(\frac{\mathbf{p}}{m_e c} \cdot \frac{\mathbf{E}}{E_S}\right)^2}, \quad (1.1)$$

where γ_e is the electron/positron Lorentz factor of momentum \mathbf{p} prior scattering, \mathbf{B} and \mathbf{E} are the magnetic and electric fields at the position of the electron. For high κ_γ the condition $\chi_e \gg 1$ must be met (Nakamura *et al.* 2012; Ridgers *et al.* 2012). Although the emission model used (Ridgers *et al.* 2013) breaks down for $\alpha\chi_e^{2/3} > 1$ (Ritus 1970; Narozhny 1979; Ilderton 2019), where $\alpha = e^2/(4\pi\epsilon_0\hbar c)$ is the fine structure constant and ϵ_0 is the vacuum permittivity, it requires laser intensities significantly higher than those used in the present work.

The e^-e^+ pair generation mechanism in section 3 is the multiphoton Breit-Wheeler process (Ehlotzky *et al.* 2009), synopsised in $\omega_\gamma + N\omega_l \rightarrow e^- + e^+$. Here, a large number of laser photons interacts with a high energy γ -photon generated earlier through multiphoton Compton scattering, and then generates an e^-e^+ pair. The probability of a γ -photon to produce a pair is governed by the parameter (Ritus 1970)

$$\chi_\gamma = \frac{\hbar\omega_l}{m_e c^2} \sqrt{\left(\frac{\mathbf{E}}{E_S} + c\hat{\mathbf{p}} \times \frac{\mathbf{B}}{E_S}\right)^2 - \left(\hat{\mathbf{p}} \cdot \frac{\mathbf{E}}{E_S}\right)^2}, \quad (1.2)$$

where $\hat{\mathbf{p}}$ is the unit vector of the γ -photon momentum.

The high fields available by the multi-PW lasers attracted the interest on γ -photon generation. An electron co-propagating with the laser field produces neither γ -photons nor e^-e^+ pairs due to the opposite contribution of the electric and magnetic terms in equation (1.1). However, in a realistic laser-foil experiment scenario the laser field is reflected on the foil front surface, changing its orientation and therefore enabling generation of γ -photons (Zhidkov *et al.* 2002; Koga *et al.* 2005; Gu *et al.* 2018). Another early approach on increasing the γ -photon yield suggested the use of two counter-propagating pulses (Bell & Kirk 2008; Kirk *et al.* 2009; Luo *et al.* 2015; Grismayer *et al.* 2016). This scheme was later generalised in the use of multiple laser beams (Vranic *et al.* 2016; Gong *et al.* 2017). The geometry of the target itself was also proven to be crucial as the formation of a preplasma enhanced γ -photon formation (Lezhnin *et al.* 2018; Wang *et al.* 2020). Other schemes employing micro-fabrication of the targets taking advantage of the reflected laser field have also been investigated (Ji *et al.* 2019; Zhang *et al.* 2021). In addition to the all-optical approach, the combination of a sub-PW laser beam with high-energy electrons is considered (Magnusson *et al.* 2019).

The theoretical framework on the absorption of the energy of a plane wave by the electrons and ions of a foil target is described in reference Vshivkov *et al.* (1998), although ignoring the energy share to generated γ -photons and consequently the effect of e^-e^+ pairs. In equation (17) of reference Vshivkov *et al.* (1998), the target thickness, l , is connected to the electron number density, n_e , through

$$\epsilon_0 = \frac{\pi n_e l}{n_{cr} \lambda}, \quad (1.3)$$

where ϵ_0 is the normalised areal density and $n_{cr} = \epsilon_0 m_e \omega^2 / e^2$ is the critical electron number density. The optimum condition for coupling the plane wave to the target is

obtained for $\epsilon_0 = a_0$, where $a_0 = eE/(m_e c \omega_l)$ is the dimensionless amplitude. For $\epsilon_0 \ll a_0$, relativistic transparency of the target results in weak coupling of the laser to the target, whilst for $\epsilon_0 \gg a_0$, the laser field is strongly reflected by the target front surface.

Equations (32) and (33) in reference Vshivkov *et al.* (1998) give the ratio of the incident (at an angle θ_0 with the target normal) to reflected wave amplitude for an s-polarised laser, $r^s = \epsilon_0/[i \cos(\theta_0) + \epsilon_0]$, and a p-polarised laser, $r^p = \epsilon_0 \cos(\theta_0)/[i + \epsilon_0 \cos(\theta_0)]$, respectively. In an AP laser, E_x is always zero; in contrary, in a RP laser E_x increases by reducing the f-number. At $\theta_0 = 90^\circ$ there is a qualitative analogy between r^s at $\theta_0 = 0^\circ$ with an AP laser on one hand, and r^p with a RP laser on the other. Therefore, at the tight-focusing scheme, an AP laser is reflected stronger than a RP laser. Up to this point, we have discussed the physical processes enabling us to study the interaction of an ultrarelativistic λ^3 -laser with a solid target via particle-in-cell (PIC) simulations.

One aspect not addressed in PIC simulation studies is the further interactions of the multi-MeV energy particles with the surrounding material, either the vacuum chamber itself or a secondary target. PIC-produced particles generate electrons through ionisation (Landau 1944) but also e^-e^+ pairs through pair production in the Coulomb field of nuclei (Bethe & Heitler 1934) and/or atomic electrons (Wheeler & Lamb Jr 1939). Post-PIC γ -photons result from either Rayleigh/Compton scattering (Compton 1923) or Bremsstrahlung emission (Koch & Motz 1959; Aichelin 1991). Furthermore, neutrons, protons, ions, and nuclides are produced through photonuclear reactions (Hayward 1970), electronuclear reactions (Budnev *et al.* 1975) and through nuclear interactions with heavy ions (Aichelin 1991). These interactions are simulated by the Monte Carlo (MC) particle transport code FLUKA (Battistoni *et al.* 2015; Böhlen *et al.* 2014) which can estimate the radioactive nuclides produced and the energy spectra of the post-PIC generated particles. These estimations are useful in nuclear waste management (199 1998), positron annihilation lifetime spectroscopy (Audet *et al.* 2021), e^-e^+ plasma studies (Chen *et al.* 2011; Sarri *et al.* 2015) and nuclear medicine (Schneider *et al.* 2002).

This paper starts with the description of our numerical solution for the laser field under the tight-focusing scheme as described in references Jeong *et al.* (2015) (for LP lasers) and Jeong *et al.* (2018) (for RP and AP lasers). Based on the choice of a single-cycle pulse, the laser focuses in a $\sim \lambda/2$ diameter sphere (λ^3 regime), for which an analytical estimation of the peak intensity is obtained. It is found that an ~ 80 PW laser leads to a peak intensity of 10^{25} Wcm^{-2} . The λ^3 regime exhibits a complex interaction with the foil target as discussed in section 3.1, regardless the great simplicity of the problem compared to multi-cycle pulses interacting with sophisticated target geometries. Sections 3.2 and 3.3 describe the evolution of γ -photon and e^-e^+ pair generation. Ballistic evolution of the γ -photons reveals a multi-PW γ -flash, expanding with preference to certain directions depending on the laser polarisation mode. A multi-parametric dependency of the laser energy transferred to each particle species is presented in sections 3.4, where the variables include the target thickness, electron number density and laser polarisation. At the optimal parameters combination, κ_γ is approaching 50 %, accompanied by a laser to positron energy conversion efficiency, κ_{e^+} , of ~ 10 %. Our results are generalised in section 3.5 for laser powers in the range $1 \text{ PW} \leq P \leq 300 \text{ PW}$, revealing a saturating trend for κ_γ , along with an optimum region of e^-e^+ pair avalanche altering the γ -photon spectrum. As a final step, in section 4 the obtained γ -flash is combined with MC simulations in the vicinity of a high-Z secondary target, to elucidate the importance of the photonuclear interactions.

2. Simulation Setup

2.1. Configuration of the λ^3 Fields

Since the paraxial approximation frequently used by default in PIC codes fails to correctly form the fields in the λ^3 regime, we followed a method where the electromagnetic fields are pre-calculated based on the tight-focusing scheme. We have obtained numerical solutions to the theory described in reference Jeong *et al.* (2015) for a LP tightly focused laser, where the validity of the model can be applied for $f_N \geq 1/4$. We have then extended our numerical solutions for a RP and AP laser, based on the theoretical solutions in reference Jeong *et al.* (2018). Here, we describe the basic steps followed in order to calculate the λ^3 -fields on focus, through a Fortran program we developed.

We assume a laser before parabola having a uniform spatial profile (a super-Gaussian profile of which the order goes to infinity) of diameter D , and that the beam is decomposed to the sum of fundamental wavelengths Böhle *et al.* (2014), corresponding to a minimum wavelength of $\lambda_{min} = 700$ nm, a maximum wavelength of $\lambda_{max} = 1750$ nm, a central wavelength of $\lambda_c = 1000$ nm and equally spaced, equally weighted wavevector intervals (for mathematical simplification) of $dk = (1/\lambda_{min} - 1/\lambda_{max})/(\lambda_{max} - \lambda_{min})$.

The integral over all wavevectors gives the electric field of the plane wave laser, as

$$E_{pw}(t) = \frac{\sin(2\pi ct/\lambda_{max}) - \sin(2\pi ct/\lambda_{min})}{t(2\pi c/\lambda_{max} - 2\pi c/\lambda_{min})}, \quad (2.1)$$

which when squared, corresponds to the intensity as plotted by the red line in figure 1(a). The envelope of the laser is obtained by the Fourier transform of the flat-top spectral power range, resulting in an electric field envelope of

$$E_{sinc}(t) = \frac{\sin[\pi ct(1/\lambda_{min} - 1/\lambda_{max})]}{\pi ct(1/\lambda_{min} - 1/\lambda_{max})}, \quad (2.2)$$

while the corresponding intensity is shown by the blue dashed line in figure 1(a) and corresponds to a pulse duration of ~ 3.4 fs at full width at half maximum (FWHM).

The calculation of electric and magnetic field components is performed in a Cartesian three-dimensional (3D) grid. Let E_{sum}^2 be the sum of the squared electric field over all grid locations, for all three Cartesian components. By setting V as the volume of each computational cell, the laser energy corresponding to the electric field is

$$\mathcal{E}_E = \frac{\varepsilon_0 E_{sum}^2}{2} V. \quad (2.3)$$

The energy contribution of the magnetic field is equal to that of the electric field, resulting in a laser energy of $\mathcal{E}_l = \varepsilon_0 E_{sum}^2 V$. By knowing the total laser energy, one can weight accordingly each fundamental frequency contribution, with a weight coefficient, W . In our specific case, $\mathcal{E}_l = 280$ J, resulting in a laser power of ~ 80 PW.

The core part of our solution is the estimation of the three electric and three magnetic field components, at each cell of a 3D computational grid. To do so, at each cell we first sum the field contribution from the incident monochromatic electric field on the focusing optic surface over the azimuthal angle ($0 \leq \phi < \pi$) and the polar angle ($\theta_{min} \leq \theta \leq \pi$, where θ_{min} is given in reference Jeong *et al.* (2015) as a function of f and D) and then sum the contribution from each fundamental wavelength. Therefore, a six-fold Do-loop with Open Multi-Processing Application Programming Interface is employed, with the layers order from outer to inner being $y \rightarrow z \rightarrow x \rightarrow \lambda \rightarrow \theta \rightarrow \phi$.

Before solving the field integrals, we calculate a set of inter-related quantities independent to the grid position, $k = 2\pi/\lambda$, $A = \sin(\theta)/[1 - \cos(\theta)]$ and $B = [1 - \cos(\theta)]/(2kf)$. Three simplification variables connected to the grid location are also calculated, $X =$

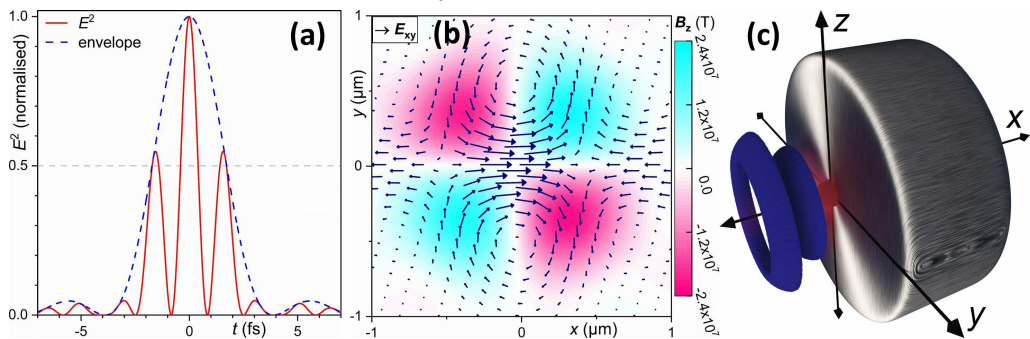


FIGURE 1. (a) The E^2 profile of the unfocused laser as a function of time is shown by the red line, as described in subsection 2.1. The blue dashed line shows the pulse envelope, with a pulse duration of ~ 3.4 fs. (b) Electromagnetic field representation of the λ^3 -laser, for the laser parameters used in this paper. The black arrows correspond to the electric field vectors, over-plotted on a contour of the magnetic field, on the xy-plane. The result is obtained after free-propagating the externally calculated fields into EPOCH, near focal position (at ~ -0.3 fs). This field corresponds to a time-averaged peak intensity of 10^{25} Wcm $^{-2}$. (c) Schematic representation of the simulation setup. The grey cylinder represents the target. The blue intensity isosurface at 2×10^{24} Wcm $^{-2}$ corresponds to the externally imported electric and magnetic fields before propagation. The red intensity isosurface (FWHM of peak intensity) shows the λ^3 -laser, corresponding to fig. 1(b).

$\{2f \cos(\theta) - x[1 - \cos(\theta)]\}/(2f)$, $Y = \{2f \sin(\theta) \cos(\phi) - y[1 - \cos(\theta)]\}/(2f)$ and $Z = \{2f \sin(\theta) \cos(\phi) - z[1 - \cos(\theta)]\}/(2f)$. Then, a phase term is calculated, $F = k[x \cos(\theta) + y \sin(\theta) \cos(\phi) + z \sin(\theta) \sin(\phi)]$.

The above expressions simplify the integrands (integrated over θ and ϕ) from references Jeong *et al.* (2015, 2018) into the form shown in appendix A for a LP laser and in appendix B for a RP laser. For an AP laser we interchange the integrands of the electric and magnetic terms. The electric field of a RP laser along the laser propagation direction is then

$$E_x = \frac{f}{\lambda_c} \sum_{\lambda=\lambda_{min}}^{\lambda_{max}} W \sum_{\phi=0}^{2\pi} \sum_{\theta=\theta_{min}}^{\pi} I_{Ex-R}, \quad (2.4)$$

(where I_{Ex-R} is given by equation (B1)) which is scaled by multiplying by $2\pi(\pi - \theta_{min})/(n_\theta n_\phi)$, where n_θ and n_ϕ is the number of elements in the θ -array and ϕ -array, respectively. By calculating E_x , E_y , E_z in all grid locations we obtain the three arrays containing the components of the electric field, whilst the same process is applied for the magnetic field calculation.

2.2. Laser Intensity in the λ^3 Regime

In order to find an approximate value of the peak laser intensity, I_p , we consider only the central peak of the electric field, as shown in figure 1(a) for -0.8 fs $\lesssim t \lesssim 0.8$ fs, containing $\sim (1/3) \mathcal{E}_l$ at FWHM (temporal profile). In addition, we consider that an Airy function corresponds to $\sim (1/2) \mathcal{E}_l$ at FWHM (spatial profile). In the λ^3 regime, the laser field corresponds to a spherical volume, V_S , of $\sim \lambda/2$ diameter. The focused fields are obtained by setting $f_N = 1/3$ in section 2.1. By combining the above, and transforming the temporal dimension in spatial, we get

$$I_p = \frac{c \mathcal{E}_l / 6}{V_S} = \frac{8c \mathcal{E}_l}{\pi \lambda^3}. \quad (2.5)$$

In this work $\mathcal{E}_l = 280 \text{ J}$ (apart section 3.5) and $\lambda = 1 \mu\text{m}$, where equation (2.5) gives $I_p \approx 2 \times 10^{25} \text{ Wcm}^{-2}$, or a most commonly used time-average intensity (or simply intensity) of $I \approx 10^{25} \text{ Wcm}^{-2}$.

The peak intensity can also be calculated in the basis of a more strict definition. The spatial boundary of the λ^3 regime corresponds to the first minima of the Airy function, which requires reduction to $\sim 83.8\% \mathcal{E}_l$. On the temporal dimension, consideration of only the central peak of the electric field (as previously) requires further reduction to $\sim 44.2\% \mathcal{E}_l$, reducing it to $\mathcal{E}_l \rightarrow 0.838 \times 0.442 \times 280 \text{ J} \approx 104 \text{ J}$.

The energy fraction contained in the sphere of Gaussian profile in all directions and of radius r and standard deviation $\sigma = \sqrt{8 \ln(2)}$ FWHM can be calculated as:

$$\int_0^{2\pi} \int_0^\pi \int_0^r \left(\sigma \sqrt{2\pi} \right)^{-3} \exp \left[-\frac{1}{2} \left(\frac{r}{\sigma} \right)^2 \right] r^2 \sin(\theta) dr d\theta d\phi = \text{erf} \left(\frac{r}{\sqrt{2}\sigma} \right) - \sqrt{\frac{2}{\pi}} \frac{r}{\sigma} \exp \left[-\frac{1}{2} \left(\frac{r}{\sigma} \right)^2 \right], \quad (2.6)$$

By dividing equation (2.6) by the volume of the sphere, taking the limit as $r \rightarrow 0$, and using L'Hospital's rule once, we estimate

$$\lim_{r \rightarrow 0} \frac{\text{erf} \left(\frac{r}{\sqrt{2}\sigma} \right) - \sqrt{\frac{2}{\pi}} \frac{r}{\sigma} \exp \left[-\frac{1}{2} \left(\frac{r}{\sigma} \right)^2 \right]}{\frac{4}{3} \pi r^3} = \frac{1}{(2\pi\sigma^2)^{3/2}}. \quad (2.7)$$

By considering the energy contained in the sphere, and transforming the spatial dimension in temporal, we obtain:

$$I_p = \frac{c(0.838 \times 0.442 \times \mathcal{E}_l)}{(2\pi\sigma^2)^{3/2}}. \quad (2.8)$$

By replacing $\sigma \approx \lambda/[4\sqrt{2 \ln(2)}]$, equation (2.8) gives:

$$I_p = \left[\sqrt{\frac{\ln(2)}{\pi}} \frac{4}{\lambda} \right]^3 c(0.838 \times 0.442 \times \mathcal{E}_l) \approx \frac{2.457 c \mathcal{E}_l}{\lambda^3}, \quad (2.9)$$

which again gives $I \approx 10^{25} \text{ Wcm}^{-2}$.

By relating the intensity to the corresponding electric field through $E = \sqrt{2I/(c\epsilon_0)}$, the focused laser gives $E \approx 8.7 \times 10^{15} \text{ Vm}^{-1}$. This field gives a value for the dimensionless amplitude of $a_0 \approx 2700$, where we further approximate $\gamma_e \approx a_0$.

2.3. PIC Simulation Setup

The results presented in this paper are obtained through 3D PIC simulations by use of the EPOCH (Arber *et al.* 2015) code. The code is compiled with the flags for Quantum Electrodynamics (QED) (Ridgers *et al.* 2014) and Higuera-Cary (HC) (Higuera & Cary 2017) preprocessor directives enabled. The QED module enables γ -photon and e^-e^+ pair generation, the inclusion of which is essential at ultra-high intensities. Since γ -photon generation is directly connected with electron/positron energy and trajectory, an accurate estimation of their motion is necessary. The HC solver accounts for the necessity of increased motion accuracy, since the default Boris (Boris 1970) solver is less reliable for relativistic particles.

No laser-block is used in our simulations. Instead, we take advantage of the EPOCH fields-block, which enables the import of a desired electromagnetic field configuration as three electric and three magnetic field components. The field data were pre-calculated (as

described in section 2.1) in a 3D grid matching the number of cells per dimension with those used in the PIC grid. In this work we define that the laser is focused at $t = 0$ fs, as shown in figure 1(b). The imported unfocused field data were calculated at $t \approx -4.27$ fs. The simulation setup shown in figure 1(c), where the imported fields are overlapped to the target geometry.

The 3D EPOCH grid is cubic, with the focal spot defined at the centre of the cube. All three dimensions extend from $-5.12 \mu\text{m}$ to $5.12 \mu\text{m}$ with 1024 cells per dimension. The resulting cells are cubes with an edge of $\alpha_c = 10$ nm. The highest electron number density used is $5 \times 10^{24} \text{ cm}^{-3}$, for which, at an intensity of 10^{25} Wcm^{-2} , the relativistically corrected skin depth is resolved with an accuracy of more than 10 cells per skin depth. At that electron number density, the skin depth can be resolved even with intensities as low as 10^{21} Wcm^{-2} . The simulation stops after 16 fs, since beyond that time fields start escaping the simulation box, for which we have set open boundary conditions. The box dimensions are chosen large enough that the laser to each particle species energy conversion efficiency, κ , saturates.

The particle species set at code initialisation are ions and electrons, while γ -photons and e^-e^+ pairs are generated during code execution. The ion atomic number is set to $Z = 1$, while its mass number at $A = 2.2$, which is the average A/Z for solid elements with $Z < 50$. EPOCH behaviour was tested for multiplying Z and A by a factor and simultaneously reducing the ion number density by the same factor, giving identical results. Therefore, our simulations can be generalised for most target materials used in laser-matter interaction experiments.

The target geometry is cylindrical, with the cylinder radius being $r = 2.4 \mu\text{m}$ and the height of the cylinder (target thickness), l , varying in the range $0.2 \mu\text{m} \leq l \leq 2 \mu\text{m}$. Although the target can be considered as mass-limited, its radius is large enough that its periphery survives the laser-foil interaction by the end of the simulation. The target front surface is placed at $x = 0 \mu\text{m}$, coinciding with the focal spot. The electron number density is uniform for each simulation, and is within the range $2 \times 10^{23} \text{ cm}^{-3} \leq n_e \leq 5 \times 10^{24} \text{ cm}^{-3}$. In order to have 8 macroparticles per cell, the number of ions and initial electrons is set to $8\pi r^2 l / \alpha_c$. Since it was found that γ -photons with energy < 1 MeV account for $\sim 1\%$ of the γ -photon energy, only those above that energy threshold were allowed in the simulation.

3. Results and Discussion

The present section provides a detailed description on the interaction of the ultra-intense laser with a solid target in the λ^3 regime, for RP, LP and AP lasers. In subsections 3.1, 3.2 and 3.3 the description is made for a relatively thick target ($2 \mu\text{m}$) with an electron number density similar to titanium ($1.2 \times 10^{24} \text{ cm}^{-3}$).

3.1. Electron Evolution

A schematic representation of the simulation setup used in the current subsection is shown in figure 1(c), where a λ^3 -pulse interacts with a $2 \mu\text{m}$ thick cylindrical target of $1.2 \times 10^{24} \text{ cm}^{-3}$ electron number density. These target parameters correspond to the highest κ_γ achieved in our simulations for an ~ 80 PW laser, approaching 50%. The interaction results in a double exponentially decaying electron spectrum for all three polarisations, where the first exponential is approximately in the energy range of $200 \text{ MeV} \leq \mathcal{E}_e \leq 500 \text{ MeV}$ and the second for $\gtrsim 500 \text{ MeV}$. The temperature of the lower energy part of the spectrum is $\sim 100 \text{ MeV}$ and approximately double for the higher energy part. These electrons are accompanied by an ion spectrum of similar temperature, a

	$e^- (\mathcal{E}_e < 500 \text{ MeV})$	$e^- (\mathcal{E}_e > 500 \text{ MeV})$	$\gamma\text{-photon } (\mathcal{E}_\gamma > 500 \text{ MeV})$
RP laser	99 MeV	204 MeV	139 MeV
LP laser	128 MeV	172 MeV	178 MeV
AP laser	96 MeV	280 MeV	147 MeV

TABLE 1. The temperature of electrons and γ -photons for a RP, a LP and an AP laser.

Maxwell-Jüttner-like positron spectrum and a γ -photon exponentially decaying spectrum of $\sim 150 \text{ MeV}$ temperature. The exact temperatures for electron and γ -photon spectra for RP, LP and AP lasers are summarised in table 1.

As mentioned earlier in section 1, one fundamental difference of a RP and an AP laser (tightly focused) is the presence and the absence of E_x , respectively (Jeong *et al.* 2018). For a LP laser of the same power, although resulting in higher intensity, E_x is weaker than that of the RP laser. For a tightly focused laser, E_x dominates over E_r , as seen by the centre of figure 1(b). Another field feature for the tight-focusing scheme is the curled field vectors centred at a distance of $\sim \lambda/2$ from focus. This pattern can be realised as an interference of the Airy pattern for a plane wave, when tightly focused. For the AP laser, the electric and magnetic field roles are interchanged, where the electric field now has a rotating form around the laser propagation axis.

Figure 1(b) reveals the complexity of the λ^3 -laser due to interplay of all three field components, versus two for weak-focusing. Furthermore, the single-cycle condition breaks the repetitive nature of a multi-cycle laser, where despite limiting the laser-foil interaction in the wavelength timescale, each time has a unique effect on the evolution of the interaction. That complicated field behaviour results in a significantly different laser-foil interaction, depending on the laser polarisation. For RP, LP and AP lasers κ is significantly different, since the electron trajectories are completely incomparable.

Let us consider the case of a RP laser. As a result of the laser-foil interaction a conical-like channel is progressively drilled on the foil target by the laser field, where the ejected electrons are either rearranged in the form of a low density pre-plasma distribution, or reshaped as thin over-dense electron fronts. The conical channel formation is mainly mandated by E_x , although its formation initiates by the pulse edges even prior the arrival of the focused pulse. The dimensions of the channel are in agreement with the pulse extent, of $\sim \lambda/2$.

The channel formation is considered in three time intervals of $t_a < -\lambda/(4c)$, $-\lambda/(4c) \leq t_b \leq \lambda/(4c)$ and $t_c > \lambda/(4c)$. At t_a , although the peak laser field has not yet reached the focal spot, a low amplitude electric field exist due to the sinc temporal profile (see figure 1(a)). Those pulses, although several orders of magnitude lower than the peak laser field, are still capable of heating and driving electrons out of the target. In addition, the field corresponding to the outer Airy disks of the main pulse is also capable of affecting the target electrons. Their combined effect is deformation of the steep flat target density profile. At -1.3 fs the target profile consists of a sub-micron under-dense region at the target front surface, followed by an over-dense 10s of nanometres thick electron pile-up and then by the rest of the intact target. At that stage a directional ring of high energy electrons also appears at $\sim 60^\circ$ to the target normal, connected with the focusing conditions ($f_N = 1/3$) of the laser field. Finally, a high energy electron population is moving along the laser propagation axis. The momentum of all electron groups is governed by a characteristic time interval of $\lambda/(4c)$.

The upper row of figure 2 shows the polar energy spectrum of electrons for three

polarisations at 0.7 fs. At t_b , the curled part of the electric field changes the directionality and distribution of the thin electron ring population, transforming it into a toroidal-like electron distribution with a torus radius of $\sim \lambda/2$, matching the centre of the curled field. Simultaneously, the peak E_x reaches the focal spot without any significant decay, since the toroidal-like electron distribution allows for a practically vacuum region for the field to propagate at. At -0.3 fs the electron energy distribution reaches energies of ~ 1 GeV. However, after a time of $\lambda/(4c)$ the pulse is reflected by the thin over-dense electron front. By the time the pulse is reflected, the electron population corresponding to the toroidal structure emerges into a closed high energy electron distribution, which can be considered as a pre-plasma at the target front surface.

Within t_b , high amplitude oscillations of the electron momentum occur. At t_c electron momentum oscillations become gradually less significant, with the electron spectrum eventually saturating. At this stage, the peak laser field is not completely reflected, but E_x starts forming a cavity beyond the over-dense electron front. Part of the laser field then reaches within the cavity, further expanding it. The initial times of this process witness instantaneous intensities an order of magnitude higher than the intensity expected on focus, due to interference of the laser fields after diffraction/reflection by the cavity walls. Although the intensity occurs only instantaneously, it was found to be $\sim 8.8 \times 10^{25} \text{ Wcm}^{-2}$ in a region approximated by a sphere of ~ 50 nm diameter, at 1.7 fs. At this stage, another electron population emerges, driven by the reflected field in the backward direction. In summary, during all stages of the laser-target interaction, electron populations at 0° , $\sim 60^\circ$, and 180° are recorded.

So far, we have given a detailed explanation of the electron evolution under the influence of a RP λ^3 -laser. For a LP λ^3 -laser, although the E_x still does exist, the lack of rotational symmetry does not allow the curled fields to take a toroidal form. Therefore, although a pre-plasma distribution is formed, it is extremely asymmetric along the laser oscillation direction. The thin over-dense electron pile-up is also asymmetric. The asymmetry is due to the initial decay of the flat target, diverting the laser into a favourable direction. Asymmetric field interference does not allow the laser to form a conical cavity, but the random nature of the process forms a macroscopically rectangle-like cavity instead.

For the case of an AP λ^3 -laser the cavity formation is simpler. The absence of E_x means that the laser can be absorbed by the target in a similar manner to a weakly focused laser, suppressing the target deformation. The deformation takes the form of an over-dense electron pile-up without pre-plasma. The pre-plasma created is also suppressed, in a region near the laser propagation axis. However, by the end of the simulation a cavity is eventually created, although by that time strong fields do not exist and κ_γ is limited, as seen in section 3.2.

3.2. γ -photon and Positron Evolution

At ultra-high laser intensities γ -photon and e^-e^+ pair generation plays an important role in the laser-target interaction. The non-trivial form of the λ^3 -field reveals a strong dependency of γ -photon and e^-e^+ pair generation every quarter-period, in connection with the altered gradient/sign of the laser field, which in extension defines the electron motion as seen in section 3.1.

The γ -photon generation can be visualised by a series of polar energy spectra diagrams. An animation for various times is provided as supplementary material in movie-1. However, since we are mainly interested in the evolution of γ -photon generation, it is more appropriate to consider the difference of every two subsequent polar diagrams, where our simulations output the data every 1 fs, a time-interval similar to the quarter-period

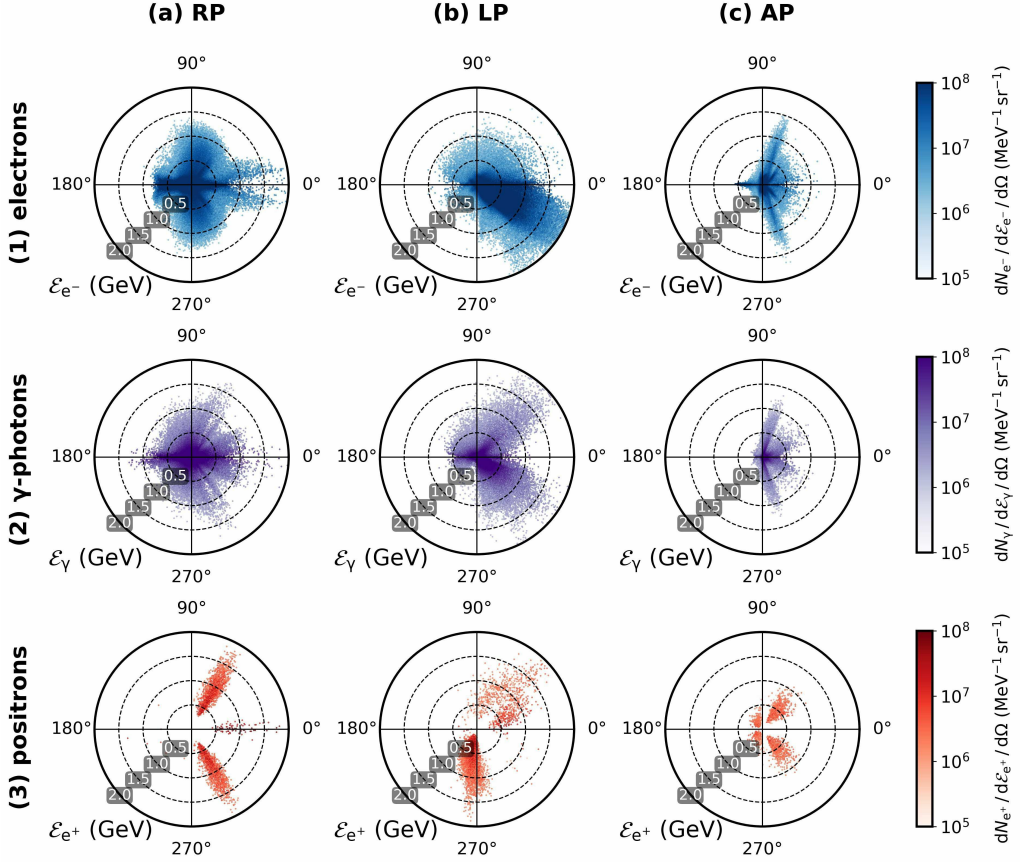


FIGURE 2. Polar energy spectrum diagrams of (1) electrons at ~ 0.7 fs. Polar energy spectrum diagrams of (2) γ -photons and (3) positrons generated in the time interval $-0.3 \text{ fs} \leq t \leq 0.7 \text{ fs}$. The figure columns correspond to (a) a RP laser, (b) a LP laser and (c) an AP laser. Animation for a larger time interval is provided in movie-1.

of 5/6 fs. The second row of figure 2 (see also the second row in movie-1) shows these diagrams for the three polarisations used, for a time interval of $-0.3 \text{ fs} \leq t \leq 0.7 \text{ fs}$. These diagrams have the benefit of not only showing at which angle γ -photons are generated at, but also a negative value exhibits γ -photon loss. In our simulations no γ -photons are allowed to escape the simulation and lack of a γ -photons is attributed only to an e^-e^+ pair formation. The corresponding plots for positrons are shown in the third row of figure 2. We must clarify that γ -photons and e^-e^+ pairs are not only formed in positive and negative polar diagram values, respectively, but a negative sign means that more γ -photons are lost to e^-e^+ pairs than what generated by the multiphoton Compton scattering process.

Let us consider a RP laser. Initially, up-to -2.3 fs , only a small fraction of electrons obtains relativistic energies due to the low amplitude periphery of the λ^3 field. These electrons then interact with the reflected relatively low amplitude edge of the laser (Ridgers *et al.* 2012) producing low energy ($\sim 0.1 \text{ GeV}$) γ -photons. However, at the next femtosecond significantly more electrons acquire relativistic energies and in combination with the increased amplitude of the field as approaching the focal spot at $\sim 60^\circ$, directional γ -photons of $\sim 0.5 \text{ GeV}$ appear at the same angle. In addition, another energetic

electron population appears towards the laser propagation axis, producing another high energy γ -photon population.

The similar process continues up-to -0.3 fs, although electric fields are intensified giving γ -photons of ~ 1 GeV. The newly generated γ -photons are still oriented purely at a $\sim 60^\circ$ cone and also on the laser axis. It is no surprise that the γ -photon yield continues increasing until the laser pulse peak amplitude reaches the focal spot. What is of a surprise is that the high energy part of the γ -photon spectrum drops near. The overall increase in κ_γ is mostly due to an isotropic generation of the moderate to low energy γ -photons.

In figure 2(c1-c3), one can observe the polar energy spectrum of positrons generated within 1 fs time interval at $\sim 60^\circ$, corresponding to the conversion of high energy γ -photons to e^-e^+ pairs. Strong e^-e^+ pair generation continues within the next two femtoseconds and then sharply decreases. This time interval is characterised by a region of negative values (γ -photon loss) in the high energy part of the γ -photon energy spectra produced within a finite time, when plotted as a function of time. This plot (not shown) reveals the quarter-period behaviour of γ -photon generation as a superposition of several peaks. As the field amplitude drops, the γ -photon production rate also drops. One can approximate the γ -photon production rate as a steep Gaussian-like function up-to the focus, followed by an exponentially-like decay.

As mentioned in section 1, a LP laser results in a higher peak intensity compared to a RP laser of the same power. Although the lack of symmetry results in a weaker coupling of the laser energy to the target electrons, the higher intensity on focus results in a slight enhancement of the high energy part of the γ -photon energy spectrum for the LP laser case. However, at energies lower than ~ 0.37 GeV the amplitude of the γ -photon energy spectrum is higher for the RP laser case. Consider that for the RP laser, γ -photons with energy $< \sim 0.37$ GeV contain $\sim 90\%$ of the γ -photon energy. Therefore, although the LP laser results in higher cut-off energies, it results in κ_γ of $\sim 40\%$, compared to $\sim 47\%$ for a RP laser. For the AP laser, although strong fields do exist, the Lorentz factor of electrons is significantly lower than the other two polarisation cases. Furthermore, no significant pre-plasma is formed in the laser field reflection region. As a result, only a κ_γ of $\sim 20\%$ occurs.

The positron spectra for LP and RP lasers overlap, apart in the very high and very low parts of the spectra, where the positrons obtain $\sim 7\%$ and $\sim 9\%$ κ_{e+} by the end of the simulation. However, this energy is not purely a result of γ -photon energy conversion to e^-e^+ pairs, but it is also a result of acceleration/deceleration of those positrons by the laser field, in the same manner as electrons (Ridgers *et al.* 2012). One index that can directly compare two interactions is the number of positrons generated, regardless their energy, where for a RP laser and a LP laser we obtain $\sim 5.7 \times 10^{11}$ positrons and $\sim 4 \times 10^{11}$ positrons, respectively. In comparison, the AP laser results in $\sim 3\%$ κ_{e+} , but generation of only $\sim 1.9 \times 10^{11}$ positrons. The imbalance of κ_{e+} to their number for the various laser polarisation modes verifies that positrons are strongly affected by the laser field after their generation.

In addition, our simulations record local positron number densities as high as $\sim 3 \times 10^{26} \text{ cm}^{-3}$, approximately two orders of magnitude higher than the titanium target electron number density, emphasizing the collective effect of e^-e^+ pairs in the laser-target interaction. By assuming that the e^-e^+ pairs are contained in a uniform density sphere of diameter equal that of the λ^3 -laser, they correspond to an average number density of $\sim 10^{25} \text{ cm}^{-3}$, still an order of magnitude higher than the target electron number density.

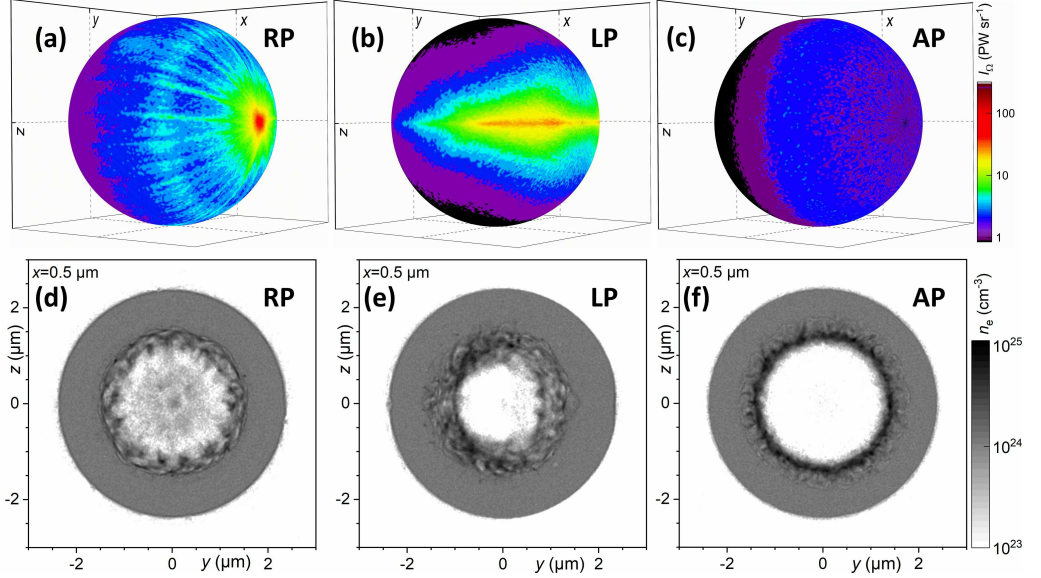


FIGURE 3. γ -photon radiant intensity for (a) a RP laser, (b) a LP laser and (c) an AP laser, 64 fs after the start of the simulation. Electron number density cross-section at $x = 0.5 \mu\text{m}$, for (d) a RP laser, (e) a LP laser and (f) an AP laser, at the end of the simulation.

3.3. γ -flash

As mentioned in reference Hadjisolomou *et al.* (2021), the γ -photons generated during the interaction of a RP λ^3 -laser with a foil appear in the form of a spherically expanding shell. The γ -photon energy density of this shell is not uniform since more energetic γ -photons are at $0^\circ, 180^\circ, \sim 60^\circ$. Computational constraints limit the γ -photon shell expansion within a cube of $\pm 5.12 \mu\text{m}$ edges. In EPOCH code, if a γ -photon is not lost to an e^-e^+ pair, then it propagates ballistically. Therefore, the γ -photon located at position $(x_{i,1}, y_{i,1}, z_{i,1})$ can propagate a distance, \mathcal{D} , to a new position, $(x_{i,2}, y_{i,2}, z_{i,2})$ (where the subscript i denotes the corresponding γ -photon of energy \mathcal{E}_i), as

$$x_{i,2} = x_{i,1} + \mathcal{D}p_{i,x} / \sqrt{p_{i,x}^2 + p_{i,y}^2 + p_{i,z}^2}, \quad (3.1)$$

$$y_{i,2} = y_{i,1} + \mathcal{D}p_{i,y} / \sqrt{p_{i,x}^2 + p_{i,y}^2 + p_{i,z}^2}, \quad (3.2)$$

$$z_{i,2} = z_{i,1} + \mathcal{D}p_{i,z} / \sqrt{p_{i,x}^2 + p_{i,y}^2 + p_{i,z}^2}, \quad (3.3)$$

which corresponds to a new distance, r_i , from the axis origin,

The ballistic γ -photon expansion for a \mathcal{D} of $15.36 \mu\text{m}$ reveals that the γ -photon population at 60° rapidly decreases geometrically. However, the γ -photon populations at $0^\circ, 180^\circ$ due to their small solid angle are preserved, as shown in figure 3(a). The spherically expanding γ -flash at large distances is considered as originating from a virtual point source, although as seen in section 3.2 the γ -photons are not generated instantaneously.

As mentioned earlier for a RP laser, γ -photons obtain $\sim 47\%$ of the $\sim 280 \text{ J}$ laser energy, or in other words, the γ -flash energy is $\sim 130 \text{ J}$. To calculate the mean location

	\mathcal{E}_γ	μ	σ	t_{FWHM}	P
RP laser	131 J	18.6 μm	0.53 μm	4.2 fs	31 PW
LP laser	113 J	18.6 μm	0.52 μm	4.1 fs	28 PW
AP laser	58 J	18.4 μm	0.58 μm	4.5 fs	13 PW

TABLE 2. Energy, mean position, position variance, duration and power of the γ -flash for a RP, a LP and an AP laser.

of the γ -flash, μ , we calculate the first order moment as

$$\mu = \frac{\sum_i \mathcal{E}_i r_i}{\sum_i \mathcal{E}_i}, \quad (3.4)$$

which for the RP laser case gives $\mu = \sim 18.5 \mu\text{m}$.

The second order moment gives the position variance, σ^2 , of the γ -flash, as

$$\sigma^2 = \frac{\sum_i \mathcal{E}_i (r_i - \mu)^2}{\sum_i \mathcal{E}_i}, \quad (3.5)$$

while the square root of the variance gives the standard deviation, which in turn gives the temporal FWHM of the γ -flash. For a RP laser the γ -flash has a FWHM duration of ~ 4.2 fs resulting in a ~ 31 PW γ -flash.

For a LP laser and an AP laser the γ -flash power is ~ 28 PW and ~ 13 PW, respectively. The AP laser results in high energy γ -photons emitted mainly at $\sim 60^\circ$, while the dominant low energy γ -photons are emitted isotropically, as shown in figure 3(c). The LP laser case results in two detached γ -photon fronts delayed by half-period, at $\sim \pm 45^\circ$ and with higher γ -photon energy density on the plane defined by the laser field oscillation. At large distances, these fronts merge, and therefore, expand as thin rings, as seen in figure 3(b). The energy, mean position, position variance, duration and power of the γ -flash for a RP, a LP and an AP laser are summarised in table 2.

The electron number density for the RP laser case forms radially symmetric regular modulations inside the target cavity [figure 3(d)]. The effect of those modulations is reflected in the γ -photon radiant intensity distribution, as shown in figure 3(a). For the LP laser case, although electron modulations are formed, they are symmetric only with respect to the laser oscillation direction [figure 3(e)]. Therefore, radial γ -photon modulations are not observed [figure 3(b)] and any γ -photon modulation is hidden by the macroscopic γ -photon distribution. For the AP laser case, radial electron modulations are formed, but with outwards directionality. Furthermore, they are shielded by the field region by an overdense electron ring distribution [figure 3(f)]. As a result, no obvious γ -photon modulations are observed.

3.4. Mapping the Energy Conversion Efficiency

In the current subsection we present the results of our multi-parametric study for an ~ 80 PW laser (RP, LP and AP laser cases) on κ_γ , κ_{e+} , laser to electron energy conversion efficiency, κ_{e-} and laser to ion energy conversion efficiency, κ_{i+} . The variable parameters include the target thickness and electron number density, for which the inversely proportional relation is mentioned in section 1. The results are presented in the form of ternary plots (West 1982) accompanied by radar charts.

Unavoidably, interaction of a laser field with matter results in transformation of a laser energy fraction to particle energy. The dependency of κ on the electron number density and target thickness can be seen in figure 4, where the direction of the grey arrow on the figure indicates increasing thickness. For both RP and LP lasers, increased laser to all particles energy conversion efficiency, $\kappa_{tot} = \kappa_{\gamma} + \kappa_{e+} + \kappa_{e-} + \kappa_{i+}$, occurs for thicker and denser targets, $\sim 80\%$ and $\sim 85\%$ for RP and LP lasers, respectively. For thinner and low density targets the particles obtain only $\sim 40\%$ of the laser energy for both RP and LP lasers (within the parameters ranges examined). For an AP laser for thin and low density targets κ_{tot} is approximately half compared to RP and LP lasers. For an AP laser (in contrary to the continuously increasing κ_{tot} behaviour for RP and LP lasers) beyond of an optimal thickness-density combination κ_{tot} starts decreasing for thicker and denser targets (maximum is $\sim 60\%$), in connection with the inefficient target cavity formation (see subsection 3.1) and increasing laser back-reflection as electron number density increases.

In general, ions being heavier than electrons, they do not produce high energy γ -photons. However, they indirectly affect the γ -photon spectrum. Their contribution arises from the amount of the laser energy transferred to them, consequently reducing electron energy and therefore what can otherwise be converted to γ -photons. For all polarisation cases κ_{i+} increases with increasing electron number density up-to an optimum value and then decreases for thicker targets (Esirkepov *et al.* 2004; Klimo *et al.* 2008; Robinson *et al.* 2008; Bulanov *et al.* 2016). Therefore, although thin targets can be dense enough to convert a large fraction of laser energy to particle energy, that energy goes primarily to ions. For thick targets, although more laser energy is converted to particle energy by increasing the electron number density, since κ_{i+} also increases, it competes with what is converted to κ_{γ} , κ_{e-} and κ_{e+} , forbidding the optimum of those particles to exist at extremely high electron number density values. For optimal thickness and density combinations, for all three polarisations, κ_{i+} reaches $\sim 25\%$.

Where κ_{i+} is not efficient, κ_{e-} and κ_{e+} cover the imbalance. For all laser polarisation modes, if the electron number density is extremely low then the laser pulse propagates through the target. Alternatively, if the target is thick enough then most of the laser energy is absorbed, resulting in enhanced κ_{e-} . For RP and LP lasers κ_{e-} is $\sim 20\%$, while for an AP laser it is $\sim 15\%$ at optimum target parameters. Some slow κ_{e-} increase for extremely high electron number densities is due to less accurate resolution of the relativistically corrected skin depth, although the increase is insignificantly small to alter the conclusion of the other particle species at that density. For RP and LP lasers, a high κ_{e-} also occurs for thin targets in regions where κ_{i+} is not efficient, due to electron capture by the laser field (Wang *et al.* 2001).

Although for an ~ 80 PW laser a significant number of e^-e^+ pairs is generated, their number is still relatively low (approximately 50 times lower) compared to the number of electrons contained in the target prior the laser-foil interaction. However, those e^-e^+ pairs are generated in regions of ultra-intense fields, therefore, stronger heated compared to the electrons in the periphery of the target cavity. The e^-e^+ pairs are more probable to originate from γ -photons of higher energy. Therefore, κ_{e+} is a combination of the energy they obtain from the Bright-Wheeler process, and to the energy due to acceleration/deceleration from the laser field. The thickness-density contour of κ_{e+} has partially topological similarities with that of κ_{i+} , meaning that positrons are affected by the laser field in a similar manner to ions. The κ_{e+} for RP and LP lasers reaches $\sim 10\%$, while it is approximately half for an AP laser. In contrary to electrons, positrons cannot obtain high κ_{e+} for under-dense thick targets because of their low generated number at these parameter values.

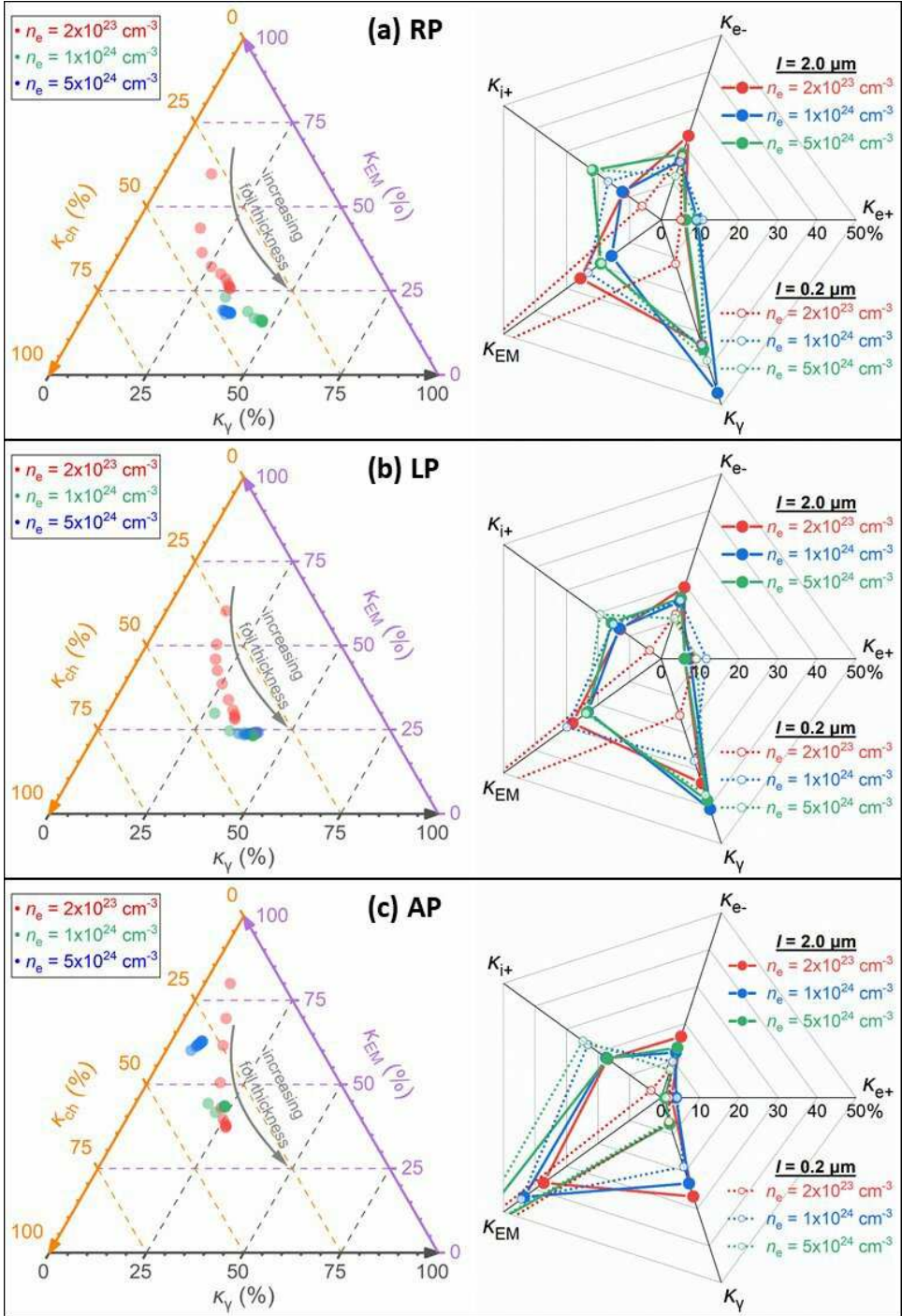


FIGURE 4. (Left) Ternary plots of κ_γ , κ_{ch} and κ_{EM} , for samples with varying electron number density and target thickness. The grey arrow points towards increasing foil thickness. (Right) Selected radar charts (solid line for $2 \mu\text{m}$ and dotted line for $0.2 \mu\text{m}$ thick foil - red for $2 \times 10^{23} \text{ cm}^{-3}$, blue for $1 \times 10^{24} \text{ cm}^{-3}$ and green for $5 \times 10^{24} \text{ cm}^{-3}$ electron number density) of κ_γ , κ_{e+} , κ_{e-} , κ_{i+} and κ_{EM} . The cases (a), (b) and (c) correspond to a RP, a LP and an AP laser, respectively.

By combining the laser to all charged particles energy conversion efficiency, $\kappa_{ch} = \kappa_{e+} + \kappa_{e-} + \kappa_{i+}$, we conclude a maximum value of $\sim 45\%$ that slowly increases by increasing target thickness, as shown in figure 4. On the other hand, the figure exhibits a steep increase of κ_γ for increasing target thickness, where the maximum values are mentioned in subsection 3.2. For a LP laser, the topology of κ_γ thickness-density contour is in agreement with that of κ_{tot} , being maximised for thick and dense targets. On the other hand, for the RP laser, although the κ_γ thickness-density contour resembles that of the LP laser for most thickness-density combinations, maximum is observed at an electron number density of $1.2 \times 10^{24} \text{ cm}^{-3}$. This local maxima is due to the different rate of energy transfer to ions, where for a RP laser it is lower at that electron number density value. In addition, κ_{tot} is slightly higher for the RP laser at thicker and denser targets, further enhancing the local maxima of κ_γ . For an AP laser, the κ_γ has an optimal electron number density at $5 \times 10^{23} \text{ cm}^{-3}$ since the lack of E_x requires a lower electron number density target for efficient laser-target coupling. For more accurate κ for each particle species at the extreme thickness-density values one is referred to the right side of figure 4.

3.5. Dependency on the Laser Power

As we have shown for an $\sim 80 \text{ PW}$ RP laser, the κ_γ is $\sim 47\%$ for targets thicker than $2 \mu\text{m}$ and an electron number density of $1.2 \times 10^{24} \text{ cm}^{-3}$. A consequent question arises on why the choice of $\sim 80 \text{ PW}$ is made and what is the effect of altering the laser power. To address that topic, the simulations for a RP laser were extended in the power range of $1 \text{ PW} \leq P \leq 300 \text{ PW}$, where the electron number density was varying in the range $10^{23} \text{ cm}^{-3} \leq n_e \leq 10^{24} \text{ cm}^{-3}$. As per the results of section 3.4, the κ_γ varies insignificantly as decreasing the electron number density from $1.2 \times 10^{24} \text{ cm}^{-3}$ to 10^{24} cm^{-3} .

Let us consider the case where the electron number density is fixed at 10^{24} cm^{-3} and the laser power varies. The κ of each species is shown in figure 5, where $a_0 \approx 307$ for 1 PW , while $a_0 \approx 5318$ for 300 PW . The κ_γ , κ_{e+} , κ_{e-} and κ_{i+} are shown with the black, red, blue and green continuous lines, respectively, while the percentage of the laser energy remaining as electromagnetic energy, κ_{EM} , is shown by the purple continuous line.

From the purple line in figure 5 one can observe that at low laser power the laser cannot be efficiently absorbed by the target and it is mostly reflected, since at low power the skin depth does not have significant relativistic increase. However, by increasing the laser power to 20 PW , corresponding to $a_0 \sim 1400$, $\sim 75\%$ of the laser energy is absorbed by the target. By further increasing the power up-to 300 PW the percentage of the laser energy absorbed increases, although with a lower rate as power increases and eventually saturating at $\sim 10\%$.

At $\sim 20 \text{ PW}$ the κ_γ , κ_{e-} and κ_{i+} becomes equally important. At $P \lesssim 5 \text{ PW}$, most of the laser energy is transferred to electrons and ions, with γ -photons and positrons obtaining an insignificantly low laser energy fraction. However, the picture reverses for $P \gtrsim 20 \text{ PW}$, where κ_{i+} saturates at $\sim 15\%$. The κ_{e-} also exhibits a plateau region at $1 \text{ PW} \lesssim P \lesssim 5 \text{ PW}$, after which, κ_{e-} continuously decreases for increasing laser power and eventually saturating at $\sim 10\%$. The κ_{e+} continuously increases for laser power up to $\sim 80 \text{ PW}$, where after obtaining a maximum value of $\sim 9\%$ it decreases to $\sim 5\%$ for higher power values.

The trend of κ_γ in figure 5 changes at $\sim 80 \text{ PW}$ power. Since κ_{e+} , κ_{e-} and κ_{i+} all saturate for increasing power, then κ_γ unavoidably also saturates, where the sum of κ_{e+} , κ_{e-} and κ_{i+} suggests a κ_γ saturation at $\sim 60\%$. Therefore, we treat the κ_γ function as the difference of a ‘‘Logistic’’ and a ‘‘LogNormal’’ function, given respectively by the left

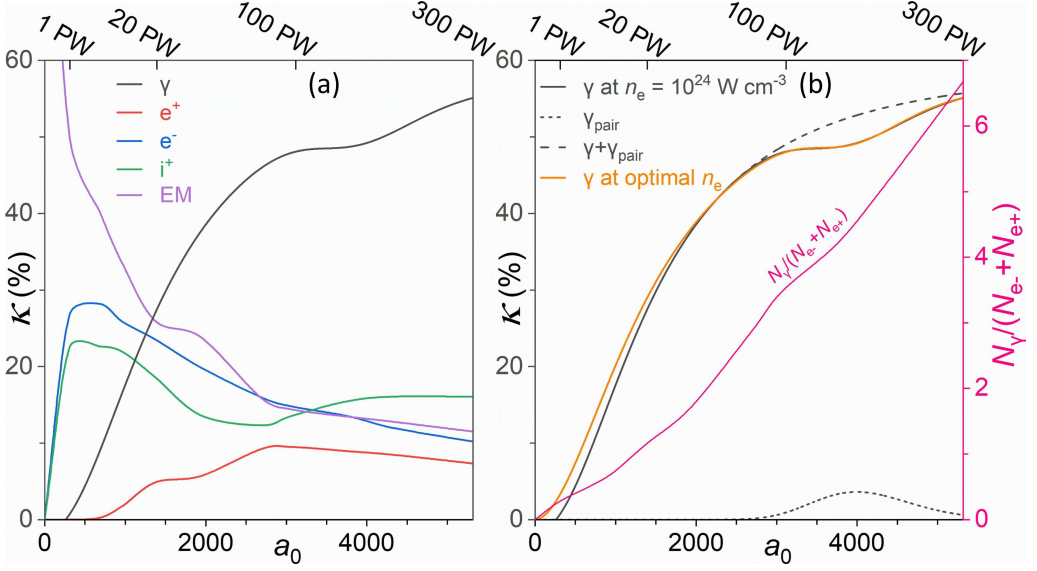


FIGURE 5. (a) κ_γ (black line), κ_{e^+} (red line), κ_{e^-} (blue line), κ_{i^+} (green line) and κ_{EM} (purple line) as a function of a_0 for a RP λ^3 -laser and an electron number density of $10^{23} - 10^{24} \text{ cm}^{-3}$; (b - left axis) κ_γ fitted with equation (3.6) for an electron number density of $10^{23} - 10^{24} \text{ cm}^{-3}$ (black solid line) and at the optimum electron number density at each power (orange line). The fitted curve is the difference of a “Logistic” (long-dashed black line) and a “LogNormal” function (short-dashed black line), as defined in the text. (b - right axis) The ratio of the γ -photon number over the sum of electron and positron number as a function of a_0 for an electron number density of $10^{23} - 10^{24} \text{ cm}^{-3}$.

and right parts of equation

$$\kappa_\gamma = A_2 + \frac{A_1 - A_2}{1 + (x/x_0)^p} - \frac{A_3}{wx} \exp \left\{ -\frac{[\ln(x/x_c)]^2}{2w^2} \right\}. \quad (3.6)$$

Fitting of equation (3.6) to κ_γ as shown in figure 5(b) gives $A_1 \approx -1.75$, $A_2 \approx 59.8$, $p \approx 2.05$, $x_0 \approx 1463$, $A_3 \approx 2213$, $w \approx -0.151$ and $x_c \approx 4088$.

The “Logistic” function [black dashed line in figure 5(b)] explains the expected κ_γ saturation for an increasing laser power. The parameter A_2 suggests κ_γ saturation at $\sim 59.8\%$, while the parameter A_1 suggests that at an electron number density of 10^{24} cm^{-3} no γ -photons can be produced for a laser power of $\sim 0.7 \text{ PW}$. The “LogNormal” function [black dotted line in figure 5(b)], having a negative sign, suggests that a γ -photon population is lost to e^-e^+ pairs, where their contribution becomes most significant for an $\sim 177 \text{ PW}$ as suggested by the parameter x_c .

By repeating the analysis described above for electron number densities in the range $10^{23} \text{ cm}^{-3} \leq n_e \leq 10^{24} \text{ cm}^{-3}$ we find the optimal electron density value at each power for maximising κ_γ , plotted by the orange line in figure 5(b). The trend suggests that a 1 PW is sufficient for a κ_γ of $\sim 3\%$. The density-power contour suggests that κ_γ is strongly dependent on the electron number density at low laser power, optimal at $2 \times 10^{23} \text{ cm}^{-3}$ for a 1 PW laser. By increasing the laser power, denser targets are required to give the peak κ_γ , although the density dependency becomes less prominent as power increases.

The pink line on the right side of figure 5(b) shows the ratio of γ -photon number produced to the sum of electron and positron number as a function of a_0 . The line exhibits an approximately linearly increasing trend, suggesting that at higher laser powers each

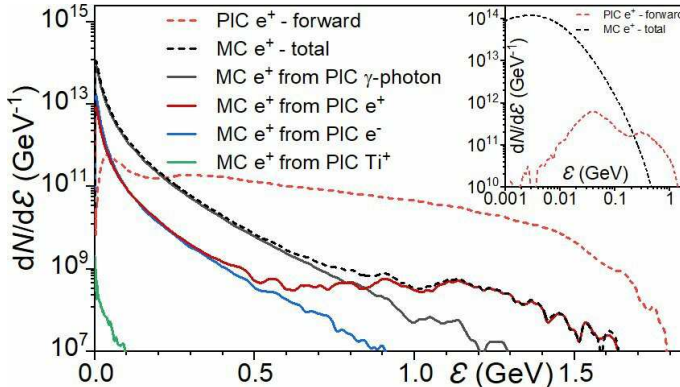


FIGURE 6. The figure shows, per λ^3 -pulse, the energy spectrum of the PIC positrons moving in the forward direction (red dashed), along with the positron spectra from the MC simulations in total (black dashed line), and separated per producing species [γ -photons (black), electrons (blue), positrons (red) and titanium ions (green)].

electron/positron can emit γ -photons several times by the end of the simulation. For an ~ 80 PW laser, each electron/positron emits γ -photons approximately three times.

4. γ -flash Interaction with High-Z target

In order to examine the effect of the γ -flash described in section 3.3 on a secondary, high-Z target, we perform MC simulations using the FLUKA code (Battistoni *et al.* 2015; Böhlen *et al.* 2014) and its graphical interface FLAIR (Vlachoudis 2009). In addition to γ -photons, the effects of the charged PIC-produced particles with the secondary target are also investigated. The PIC output particles (type, position, momentum and weight) are imported to FLUKA as primary particles. The secondary target is modelled as a 10 mm thick disk of 100 mm diameter and it is located at 0.1 mm from the focal spot coordinates. The large acceptance angle covered by the secondary target allows to intercept almost all PIC generated particles in the forward direction. Natural lead, Pb, is chosen as material for the disk because of its high cross section for pair production and photonuclear interactions for energies considered. For the simulations, the FLUKA PRECISIO defaults are used. Additionally, the electromagnetic transport thresholds are set at 0.1 MeV, the photonuclear and electronuclear interactions are enabled, as well as the evaporation of heavy fragments and nuclear coalescence.

Figure 6 shows that the PIC generated positrons moving in the forward direction, exhibiting a rather flat spectrum with a temperature of ~ 0.4 GeV. The figure overplots the spectra of positrons escaping the secondary target in the forward direction, obtained from the MC simulations, integrated (black dashed line) and separated per each primary particle species (solid lines), namely γ -photons, electrons, positrons and titanium ions. From figure 6 it is seen that the largest number of positrons ($\sim 81.4\%$) is produced by γ -photons and that the most energetic positrons are those directly created in the PIC simulations.

Positrons produced by PIC γ -photons and electrons have a temperature of ~ 0.1 GeV. The positron population exhibits two temperatures, the first of ~ 0.1 GeV corresponding to those generated in the lead target, and the second at higher temperature corresponding to PIC generated positrons. The low temperature positrons are generated via e^-e^+ pair production from Bremsstrahlung γ -photons. The positron spectra after the secondary

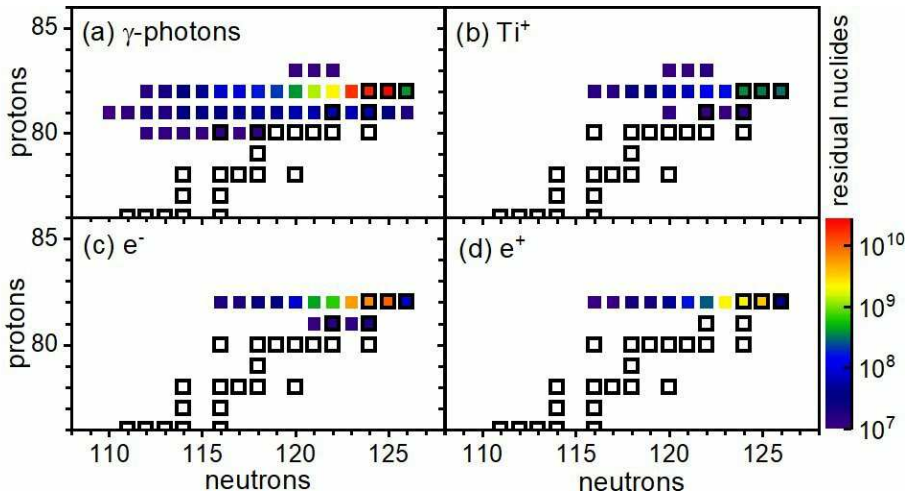


FIGURE 7. Chart of residual nuclides obtained from MC simulation per λ^3 -pulse and separated per each PIC particle species. Stable nuclides are highlighted with a box.

target is shifted towards lower energy with respect to the PIC-produced positrons, while their total number is increased by approximately an order of magnitude.

MC simulations also allow to estimate the number of stable and unstable nuclides generated in the lead target. Figure 7 shows the chart of the produced nuclides focused around the lead position and separated per each PIC particle species. Stable nuclides are highlighted with a box. Most of the residual nuclides are produced through photonuclear interactions, either directly by primary (PIC) γ -photons or indirectly by secondary (Bremsstrahlung from fast electrons/positrons) γ -photons. In our γ -photon energy region of interest, the Giant Dipole Resonance (GDR) photonuclear process dominates since it has the highest integrated cross section, peaking at ~ 13.6 MeV γ -photons. Apart of photonuclear interactions, residual nuclides can be also produced by nucleus-nucleus interactions and/or electronuclear interactions.

One of the most abundant generated lead isotopes is $^{203}_{82}\text{Pb}$ where $\sim 10^9$ nuclides are produced with a half life of ~ 52 h. Its direct decay to $^{203}_{81}\text{Tl}$ (stable) through electron capture and it does not emit any hadrons. In addition, photons of ~ 279.2 keV are emitted which are particularly suitable for medical imaging (Azzam *et al.* 2014). The second most abundant isotope produced is thallium, with $^{201}_{81}\text{Tl}$ ($\sim 10^8$ nuclides) being historically used extensively for nuclear medicine (Tadamura *et al.* 1999) due to its decay to $^{201}_{80}\text{Hg}$ (stable) through electron capture with a half-life of ~ 73 h.

5. Summary and Conclusions

In this work we study the highly efficient γ -photon generation through the ultra-intense laser and solid target interaction. We employ the λ^3 regime, where a single-cycle laser ~ 80 PW laser pulse is focused to a $\sim \lambda/2$ diameter sphere. The benefit of the λ^3 regime is that it provides the highest intensity achievable at a given laser power, in expense of the least energy. In this paper we study the interaction of a λ^3 -laser with matter in the QED regime, where a copious number of γ -photons and e^- - e^+ pairs is generated. The QED processes are studied by use of the 3D EPOCH PIC code. The λ^3 -laser fields are imported into EPOCH after calculated independently through our code developed.

Our work examines the laser-target interaction under RP, LP and AP lasers. A multi-

parametric study is presented, where the variables include the target thickness and electron number density. It is found that the optimal κ_γ reaches $\sim 47\%$ and it occurs for a RP laser at a target thickness of $2\ \mu\text{m}$ and an electron number density of $1.2 \times 10^{24}\ \text{cm}^{-3}$. For the same target parameters, the LP and AP lasers results in a κ_γ of $\sim 40\%$ and $\sim 20\%$, respectively. At the optimal target variables, the LP lasers gives a κ_γ of $\sim 42\%$, while the AP laser gives a κ_γ of $\sim 29\%$.

The significantly higher κ_γ for the RP laser is due to the dominance of the longitudinal, E_x field, that increases the coupling of the laser to the target. For the LP laser the E_x is smaller, where for the AP laser is absent. The E_x assists in the formation of a target cavity, where the cavity propagation performs a different propagation depending on the laser polarisation mode. Interference of the reflected/diffracted laser field inside the cavity results in an instantaneous intensity as high as $\sim 8.8 \times 10^{25}\ \text{Wcm}^{-2}$, approximately one order of magnitude higher than the intensity expected on focus.

The directionality of electrons at several instances is identified, resulting in several high energy electron groups directed at $\sim 0^\circ$, $\sim 180^\circ$ and $\sim 60^\circ$ for a RP laser. Those electrons are connected to the γ -photon directionality, being at the same angles. The ultra-high intensities employed, result in not only a prolific γ -photon generation but unavoidably to also e^-e^+ pair generation through the multi-photon Breit-Wheeler process. The generation positions of e^-e^+ pairs is identified to overlap the regions of high-energy γ -photons.

At a time of $\sim \lambda/(2c)$ after the peak of the laser pulse reaches the focal spot, the γ -photons expand radially in a ballistic fashion without significant losses to e^-e^+ pairs. The γ -photons expand within a spherical shell where the FWHM of their energy density is approximately equal to the laser wavelength, similar to the laser-foil interaction time. The expanding spherical shell for the RP, LP and AP laser results in a γ -flash of $\sim 31\ \text{PW}$, $\sim 28\ \text{PW}$ and $\sim 13\ \text{PW}$, respectively. Although a preferred directionality exists for the γ -photons, the radiant intensity of the population at $\sim 60^\circ$ is less significant due to its large solid angle, in contrary to γ -photons at $\sim 0^\circ$ and $\sim 180^\circ$.

Our analysis is also extended on varying the laser power in the range $1\ \text{PW} \leq P \leq 300\ \text{PW}$. We demonstrate that κ_γ sharply increases up to $\sim 80\ \text{PW}$, while γ -photons become the dominant species above $\sim 20\ \text{PW}$. For low laser powers strong dependency of the κ_γ exists on the electron number density, where the optimal electron number density increases approximately linearly with a_0 . For higher power values this dependency becomes less important. When increasing the laser power then the κ_γ increases, saturating at $\sim 60\%$. A κ_γ discontinuity exists centred at $\sim 177\ \text{PW}$, attributed to the γ -photon conversion to e^-e^+ pairs, while as power further increases the γ -photon reduction is compensated by further γ -photon emission by positrons, in the same manner as by electrons. In addition, as laser power increases then the number of γ -photon emission from each electron/positron also increases in an approximately linear fashion with a_0 .

Finally, for the RP laser, the interaction of the PIC generated particles interacting with a high-Z target is studied by MC simulations. The spectra of each particle species escaping the secondary target are obtained. The PIC spectra are substantially altered by the interaction with the high-Z target. The γ -flash interaction with the secondary target also results in significant production of radioactive nuclides, whose yields are estimated. Hence, the coupling of PIC and MC simulations provides a powerful tool for further investigating the laser interaction with matter.

The authors would like to acknowledge useful communication with Dr. D. Khikhlikha and K. Lezhnin. This work is supported by the projects High Field Initiative

(CZ.02.1.01/0.0/0.0/15_003/0000449) from the European Regional Development Fund and “e-INFRA CZ” (ID:90140) from the Ministry of Education, Youth and Sports of the Czech Republic. CPR would like to acknowledge funding from EPSRC, grant no. EP/V049461/1. The EPOCH code is in part funded by the UK EPSRC grants EP/G054950/1, EP/G056803/1, EP/G055165/1 and EP/M022463/1.

Appendix A.

The imaginary part of the integrands used for the electric and magnetic field calculation (Jeong *et al.* 2015) of a LP laser, as used in our Fortran code. The definition of symbols is found in section 2.1. The electric field integrands are

$$I_{Ex-L} = -A^2 B \cos(\phi) X \cos(F) + [A^2 \cos(\phi) - A^2 \cos(\phi) X] \sin(F) \quad (\text{A } 1)$$

$$I_{Ey-L} = -A^2 B \cos(\phi) Y \cos(F) + [A - A^2 \cos(\phi) Y] \sin(F) \quad (\text{A } 2)$$

$$I_{Ez-L} = -A^2 B \cos(\phi) Z \cos(F) - [A^2 \cos(\phi) Z] \sin(F) \quad (\text{A } 3)$$

The magnetic field integrands are

$$I_{Bx-L} = ABZ \cos(F) + AZ \sin(F) \quad (\text{A } 4)$$

$$I_{By-L} = -A^2 B \cos(\phi) Z \cos(F) - [A^2 \cos(\phi) Z] \sin(F) \quad (\text{A } 5)$$

$$I_{Bz-L} = [A^2 B \cos(\phi) Y - ABX] \cos(F) + [A^2 \cos(\phi) Y - AX] \sin(F) \quad (\text{A } 6)$$

Appendix B.

The imaginary part of the integrands used for the electric and magnetic field calculation (Jeong *et al.* 2018) of a RP laser, as used in our Fortran code. The definition of symbols is found in section 2.1. The electric field integrands are

$$I_{Ex-R} = A^2 BX \sin(F) - [A^2 X - A^2] \cos(F) \quad (\text{B } 1)$$

$$I_{Ey-R} = A^2 BY \sin(F) - [A^2 Y - A \cos(\phi)] \cos(F) \quad (\text{B } 2)$$

$$I_{Ez-R} = A^2 BZ \sin(F) - [A^2 Z - A \sin(\phi)] \cos(F) \quad (\text{B } 3)$$

The magnetic field integrands are

$$I_{Bx-R} = 0 \quad (\text{B } 4)$$

$$I_{By-R} = A[\sin(\phi)X - AZ] \cos(F) - AB[\sin(\phi)X - AZ] \sin(F) \quad (\text{B } 5)$$

$$I_{Bz-R} = -A[\cos(\phi)X - AY] \cos(F) + AB[\cos(\phi)X - AY] \sin(F) \quad (\text{B } 6)$$

REFERENCES

- 1998 *Accelerator Driven Systems: Energy Generation and Transmutation of Nuclear Waste: Status Report. TECDOC Series 985*. Vienna: INTERNATIONAL ATOMIC ENERGY AGENCY.
- AHARONIAN, F., AN, Q., AXIKEGU, BAI, L. X., BAI, Y. X., BAO, Y. W., BASTIERI, D., BI, X. J., BI, Y. J. & CAI, H. ET AL. 2021 Extended Very-High-Energy Gamma-Ray Emission Surrounding PSR J0622 + 3749 Observed by LHAASO – KM2A. *Phys. Rev. Lett.* **126**, 241103.
- AICHELIN, J. 1991 “Quantum” molecular dynamics—a dynamical microscopic n-body approach to investigate fragment formation and the nuclear equation of state in heavy ion collisions. *Phys. Reports* **202** (5), 233–360.
- APRIL, A. & PICHÉ, M. 2010 4π Focusing of TM01 beams under nonparaxial conditions. *Opt. Express* **18** (21), 22128–22140.
- ARBER, T. D., BENNETT, K., BRADY, C. S., LAWRENCE-DOUGLAS, A., RAMSAY, M. G., SIRCOMBE, N. J., GILLIES, P., EVANS, R. G., SCHMITZ, H. & BELL, A. R. ET AL. 2015 Contemporary particle-in-cell approach to laser-plasma modelling. *Plasma Phys. Control. Fusion* **57** (11), 113001.
- AUDET, T. L., ALEJO, A., CALVIN, L., CUNNINGHAM, M. H., FRAZER, G. R., NERSISYAN, G., PHIPPS, M. L., WARWICK, J. R., SARRI, G. & HAFZ, N. A. M. ET AL. 2021 Ultrashort, MeV-scale laser-plasma positron source for positron annihilation lifetime spectroscopy. *Phys. Rev. Accel. Beams* **24**, 073402.
- AZZAM, A., SAID, S. A. & AL-ABYAD, M. 2014 Evaluation of different production routes for the radio medical isotope ^{203}Pb using TALYS 1.4 and EMPIRE 3.1 code calculations. *Appl. Radiat. Isot.* **91**, 109–113.
- BAHK, S. W., ROUSSEAU, P., PLANCHON, T. A., CHVYKOV, V., KALINTCHENKO, G., MAKSIMCHUK, A., MOUROU, G. A. & YANOVSKY, V. 2004 Generation and characterization of the highest laser intensities (1022 W/cm²). *Opt. Lett.* **29** (24), 2837–2839.
- BATTISTONI, G., BOEHLEN, T., CERUTTI, F., CHIN, P. W., ESPOSITO, L. S., FASSÒ, A., FERRARI, A., LECHNER, A., EMPL, A. & MAIRANI, A. ET AL. 2015 Overview of the FLUKA code. *Ann. Nucl. Energy* **82**, 10–18.
- BELL, A. R. & KIRK, JOHN G. 2008 Possibility of Prolific Pair Production with High-Power Lasers. *Phys. Rev. Lett.* **101**, 200403.
- BERESTETSKII, V. B., LIFSHITZ, E. M. & PITAEVSKII, L. P. 1982 *Quantum Electrodynamics (Second Edition)*, second edition edn. Oxford: Butterworth-Heinemann.
- BETHE, H. & HEITLER, W. 1934 On the Stopping of Fast Particles and on the Creation of Positive Electrons. *Proc. R. Soc. Lond. A* **146** (856), 83–112.
- BÖHLE, F., KRETSCHMAR, M., JULLIEN, A., KOVACS, M., MIRANDA, M., ROMERO, R., CRESPO, H., MORGNER, U., SIMON, P. & LOPEZ-MARTENS, R. ET AL. 2014 Compression of CEP-stable multi-mJ laser pulses down to 4 fs in long hollow fibers. *Laser Phys. Lett.* **11** (9), 095401.
- BÖHLEN, T. T., CERUTTI, F., CHIN, M. P. W., FASSÒ, A., FERRARI, A., ORTEGA, P. G., MAIRANI, A., SALA, P. R., SMIRNOV, G. & VLACHOUDIS, V. 2014 The FLUKA Code: Developments and Challenges for High Energy and Medical Applications. *Nucl. Data Sheets* **120**, 211–214.
- BORIS, J. P. 1970 Relativistic plasma simulation-optimization of a hybrid code. *Proceeding of Fourth Conference on Numerical Simulations of Plasmas* pp. 3–67.
- BUDNEV, V. M., GINZBURG, I. F., MELEDIN, G. V. & SERBO, V. G. 1975 The two-photon particle production mechanism. Physical problems. Applications. Equivalent photon approximation. *Phys. Reports* **15** (4), 181–282.
- BULANOV, S. S., ESAREY, E., SCHROEDER, C. B., BULANOV, S. V., ESIRKEPOV, T. Z., KANDO, M., PEGORARO, F. & LEEMANS, W. P. 2016 Radiation pressure acceleration: The factors limiting maximum attainable ion energy. *Phys. Plasmas* **23** (5), 056703.
- BULANOV, S. S., ESIRKEPOV, T. Z., KAMENETS, F. F. & PEGORARO, F. 2006 Single-cycle high-intensity electromagnetic pulse generation in the interaction of a plasma wakefield with regular nonlinear structures. *Phys. Rev. E* **73**, 036408.
- BULANOV, S. V., ESIRKEPOV, T. Z., KANDO, M., KOGA, J., KONDO, K. & KORN, G. 2015

- On the problems of relativistic laboratory astrophysics and fundamental physics with super powerful lasers. *Plasma Phys. Rep.* **41**, 1–51.
- CHEN, H., MEYERHOFER, D. D., WILKS, S. C., CAUBLE, R., DOLLAR, F., FALK, K., GREGORI, G., HAZIM, A., MOSES, E. I. & MURPHY, C. D. ET AL. 2011 Towards laboratory produced relativistic electron–positron pair plasmas. *High Energy Density Phys.* **7** (4), 225–229.
- CHENG, Z., ZHOU, Y., XIA, M., LI, W., YANG, K. & ZHOU, Y. 2015 Tight focusing of the azimuthally polarized light beam for a sharper spot. *Opt. Laser Technol.* **73**, 77–81.
- COMPTON, A. H. 1923 A Quantum Theory of the Scattering of X-rays by Light Elements. *Phys. Rev.* **21**, 483–502.
- DANSON, C. N., HAEFNER, C., BROMAGE, J., BUTCHER, T., CHANTELOUP, J. F., CHOWDHURY, E. A., GALVANAUSKAS, A., GIZZI, L. A., HEIN, J. & HILLIER, D. I. ET AL. 2019 Petawatt and exawatt class lasers worldwide. *High Power Laser Sci.* **7**, e54.
- DORN, R., QUABIS, S. & LEUCHS, G. 2003 Sharper Focus for a Radially Polarized Light Beam. *Phys. Rev. Lett.* **91**, 233901.
- EHLOTZKY, F., KRAJEWSKA, K. & KAMIŃSKI, J. Z. 2009 Fundamental processes of quantum electrodynamics in laser fields of relativistic power. *Rep. Prog. Phys.* **72** (4), 046401.
- ELIASSEN, B. & LIU, C. S. 2013 An electromagnetic gamma-ray free electron laser. *J. Plasma Phys.* **79** (6), 995–998.
- ESIRKEPOV, T. Z., BORGHESI, M., BULANOV, S. V., MOUROU, G. & TAJIMA, T. 2004 Highly Efficient Relativistic-Ion Generation in the Laser-Piston Regime. *Phys. Rev. Lett.* **92**, 175003.
- GHOTRA, H. S. & KANT, N. 2015 Sensitiveness of axial magnetic field on electron acceleration by a radially polarized laser pulse in vacuum. *Opt. Commun.* **356**, 118–122.
- GONG, Z., HU, R. H., SHOU, Y. R., QIAO, B., CHEN, C. E., HE, X. T., BULANOV, S. S., ESIRKEPOV, T. ZH., BULANOV, S. V. & YAN, X. Q. 2017 High-efficiency γ -ray flash generation via multiple-laser scattering in ponderomotive potential well. *Phys. Rev. E* **95**, 013210.
- GRISMAYER, T., VRANIC, M., MARTINS, J. L., FONSECA, R. A. & SILVA, L. O. 2016 Laser absorption via quantum electrodynamics cascades in counter propagating laser pulses. *Phys. Plasmas* **23** (5), 056706.
- GU, Y. J., KLIMO, O., BULANOV, S. V. & WEBER, S. 2018 Brilliant gamma-ray beam and electron–positron pair production by enhanced attosecond pulses. *Commun. Phys.* **1**, 1–9.
- HADJISOLOMOU, P., JEONG, T. M., VALENTA, P., KORN, G. & BULANOV, S. V. 2021 Gamma-ray flash generation in irradiating a thin foil target by a single-cycle tightly focused extreme power laser pulse. *Phys. Rev. E* **104**, 015203.
- HAYWARD, E. 1970 *Photonuclear Reactions*. Washington, D.C., USA: National Bureau of Standards.
- HIGUERA, A. V. & CARY, J. R. 2017 Structure-preserving second-order integration of relativistic charged particle trajectories in electromagnetic fields. *Phys. Plasmas* **24** (5), 052104.
- ILDERTON, A. 2019 Note on the conjectured breakdown of QED perturbation theory in strong fields. *Phys. Rev. D* **99**, 085002.
- JEONG, T. M., BULANOV, S. V., WEBER, S. & KORN, G. 2018 Analysis on the longitudinal field strength formed by tightly-focused radially-polarized femtosecond petawatt laser pulse. *Opt. Express* **26** (25), 33091–33107.
- JEONG, T. M., WEBER, S., LE GARREC, B., MARGARONE, D., MOCEK, T. & KORN, G. 2015 Spatio-temporal modification of femtosecond focal spot under tight focusing condition. *Opt. Express* **23** (9), 11641–11656.
- JI, L. L., SNYDER, J. & SHEN, B. F. 2019 Single-pulse laser-electron collision within a micro-channel plasma target. *Plasma Phys. Control. Fusion* **61** (6), 065019.
- KIRK, J. G., BELL, A. R. & ARKA, I. 2009 Pair production in counter-propagating laser beams. *Plasma Phys. Control. Fusion* **51** (8), 085008.
- KLIMO, O., PSIKAL, J., LIMPOUCH, J. & TIKHONCHUK, V. T. 2008 Monoenergetic ion beams from ultrathin foils irradiated by ultrahigh-contrast circularly polarized laser pulses. *Phys. Rev. ST Accel. Beams* **11**, 031301.

- KOCH, H. W. & MOTZ, J. W. 1959 Bremsstrahlung Cross-Section Formulas and Related Data. *Rev. Mod. Phys.* **31**, 920–955.
- KOGA, J., ESIRKEPOV, T. Z. & BULANOV, S. V. 2005 Nonlinear Thomson scattering in the strong radiation damping regime. *Phys Plasmas* **12** (9), 093106.
- LANDAU, L. 1944 On the energy loss of fast particles by ionization. *J. Phys. USSR* **8** (1-6), 201–205.
- LEZHNNIN, K. V., SASOROV, P. V., KORN, G. & BULANOV, S. V. 2018 High power gamma flare generation in multi-petawatt laser interaction with tailored targets. *Phys. Plasmas* **25** (12), 123105.
- LI, J. X., SALAMIN, Y. I., GALOW, B. J. & KEITEL, C. H. 2012 Acceleration of proton bunches by petawatt chirped radially polarized laser pulses. *Phys. Rev. A* **85**, 063832.
- LI, Z., KATO, Y. & KAWANAKA, J. 2021 Simulating an ultra-broadband concept for Exawatt-class lasers. *Sci. Rep.* **11** (151).
- LUO, W., ZHU, Y. B., ZHUO, H. B., MA, Y. Y., SONG, Y. M., ZHU, Z. C., WANG, X. D., LI, X. H., TURCU, I. C. E. & CHEN, M. 2015 Dense electron-positron plasmas and gamma-ray bursts generation by counter-propagating quantum electrodynamics-strong laser interaction with solid targets. *Physics of Plasmas* **22** (6), 063112.
- MAGNUSSON, J., GONOSKOV, A., MARKLUND, M., ESIRKEPOV, T. Z., KOGA, J. K., KONDO, K., KANDO, M., BULANOV, S. V., KORN, G. & BULANOV, S. S. 2019 Laser-Particle Collider for Multi-GeV Photon Production. *Phys. Rev. Lett.* **122**, 254801.
- MOUROU, G., CHANG, Z., MAKSIMCHUK, A., NEES, J., BULANOV, S. V., BYCHENKOV, V. Y., ESIRKEPOV, T. Z., NAUMOVA, N. M., PEGORARO, F. & RUHL, H. 2002 On the design of experiments for the study of relativistic nonlinear optics in the limit of single-cycle pulse duration and single-wavelength spot size. *Plasma Phys. Rep.* **28**, 12–27.
- MOUROU, G. A., TAJIMA, T. & BULANOV, S. V. 2006 Optics in the relativistic regime. *Rev. Mod. Phys.* **78**, 309–371.
- NAKAMURA, T., KOGA, J. K., ESIRKEPOV, T. Z., KANDO, M., KORN, G. & BULANOV, S. V. 2012 High-Power γ -Ray Flash Generation in Ultraintense Laser-Plasma Interactions. *Phys. Rev. Lett.* **108**, 195001.
- NAROZHNY, N. B. 1979 Radiation corrections to quantum processes in an intense electromagnetic field. *Phys. Rev. D* **20**, 1313–1320.
- NEDOREZOV, V. G., TURINGE, A. A. & SHATUNOV, Y. M. 2004 Photonuclear experiments with Compton-backscattered gamma beams. *Phys.-Uspekhi* **47** (4), 341–358.
- OSVAY, K., BÖRZSÖNYI, A., CAO, H., CORMIER, E., CSONTOS, J., JÓJÁRT, P., KALASHNIKOV, M., KISS, B., LÓPEZ-MARTENS, R. & TÓTH, S. ET AL. 2019 Development status and operation experiences of the few cycle high average power lasers of ELI-ALPS (Conference Presentation). In *Short-pulse High-energy Lasers and Ultrafast Optical Technologies* (ed. Pavel Bakule & Constantin L. Haefner), , vol. 11034. International Society for Optics and Photonics, SPIE.
- OUILLE, M., VERNIER, A., BÖHLE, F., BOCUM, M., JULLIEN, A., LOZANO, M., ROUSSEAU, J. P., CHENG, Z., GUSTAS, D. & BLUMENSTEIN, A. ET AL. 2020 Relativistic-intensity near-single-cycle light waveforms at kHz repetition rate. *Light Sci. Appl.* **9**.
- PAYEUR, S., FOURMAUX, S., SCHMIDT, B. E., MACLEAN, J. P., TCHERVENKOV, C., LÉGARÉ, F., PICHÉ, M. & KIEFFER, J. C. 2012 Generation of a beam of fast electrons by tightly focusing a radially polarized ultrashort laser pulse. *Appl. Phys. Lett.* **101** (4), 041105.
- PERRY, M. D., PENNINGTON, D., STUART, B. C., TIETBOHL, G., BRITEN, J. A., BROWN, C., HERMAN, S., GOLICK, B., KARTZ, M., MILLER, J. & ET AL. 1999 Petawatt laser pulses. *Opt. Lett.* **24** (3), 160–162.
- PHILIPPOV, A. A. & SPITKOVSKY, A. 2018 Ab-initio Pulsar Magnetosphere: Particle Acceleration in Oblique Rotators and High-energy Emission Modeling. *Astrophys. J.* **855** (2), 94.
- PIROZHKOV, A. S., FUKUDA, Y., NISHIUCHI, M., KIRIYAMA, H., SAGISAKA, A., OGURA, K., MORI, M., KISHIMOTO, M., SAKAKI, H. & DOVER, N. P. ET AL. 2017 Approaching the diffraction-limited, bandwidth-limited Petawatt. *Opt. Express* **25** (17), 20486–20501.
- REES, M. J. & MÉSZÁROS, P. 1992 Relativistic fireballs: energy conversion and time-scales. *Mon. Not. R. Astron. Soc.* **258** (1), 41P–43P.
- RICHARDS, B., WOLF, E. & GABOR, D. 1959 Electromagnetic diffraction in optical systems,

- II. Structure of the image field in an aplanatic system. *Proceedings of the Royal Society of London. Series A. Mathematical and Physical Sciences* **253** (1274), 358–379.
- RIDGERS, C. P., BRADY, C. S., DUCLOUS, R., KIRK, J. G., BENNETT, K., ARBER, T. D. & BELL, A. R. 2013 Dense electron-positron plasmas and bursts of gamma-rays from laser-generated quantum electrodynamic plasmas. *Phys. Plasmas* **20** (5), 056701.
- RIDGERS, C. P., BRADY, C. S., DUCLOUS, R., KIRK, J. G., BENNETT, K., ARBER, T. D., ROBINSON, A. P. L. & BELL, A. R. 2012 Dense Electron-Positron Plasmas and Ultraintense γ rays from Laser-Irradiated Solids. *Phys. Rev. Lett.* **108**, 165006.
- RIDGERS, C. P., KIRK, J. G., DUCLOUS, R., BLACKBURN, T. G., BRADY, C. S., BENNETT, K., ARBER, T. D. & BELL, A. R. 2014 Modelling gamma-ray photon emission and pair production in high-intensity laser-matter interactions. *J. Comput. Phys.* **260**, 273–285.
- RITUS, V. I. 1970 Radiative Effects and Their Enhancement in an Intense Electromagnetic Field. *J. Exp. Theor. Phys.* **30** (6), 1181.
- RIVAS, D. E., BOROT, A., CARDENAS, D. E., MARCUS, G., GU, X., HERRMANN, D., XU, J., TAN, J., KORMIN, D. & MA, G. ET AL. 2017 Next Generation Driver for Attosecond and Laser-plasma Physics. *Sci. Rep.* **7**.
- ROBINSON, A. P. L., ZEPF, M., KAR, S., EVANS, R. G. & BELLEI, C. 2008 Radiation pressure acceleration of thin foils with circularly polarized laser pulses. *New J. Phys.* **10** (1), 013021.
- SALAMIN, Y. I. 2006 Fields of a radially polarized Gaussian laser beam beyond the paraxial approximation. *Opt. Lett.* **31** (17), 2619–2621.
- SALAMIN, Y. I. 2010a Direct particle acceleration by two identical crossed radially polarized laser beams. *Phys. Rev. A* **82**, 013823.
- SALAMIN, Y. I. 2010b Low-diffraction direct particle acceleration by a radially polarized laser beam. *Phys. Lett. A* **374** (48), 4950–4953.
- SALAMIN, Y. I. 2015 Fields and propagation characteristics in vacuum of an ultrashort tightly focused radially polarized laser pulse. *Phys. Rev. A* **92**, 053836.
- SALES, T. R. M. 1998 Smallest Focal Spot. *Phys. Rev. Lett.* **81**, 3844–3847.
- SARRI, G., PODER, K., COLE, J. M., SCHUMAKER, W., DI PIAZZA, A., REVILLE, B., DZELZAINIS, T., DORIA, D., GIZZI, L. A. & GRITTANI, G. ET AL. 2015 Generation of neutral and high-density electron-positron pair plasmas in the laboratory. *Nat. Commun.* **6** (6747), 1–8.
- SCHNEIDER, U., AGOSTEO, S., PEDRONI, E. & BESSERER, J. 2002 Secondary neutron dose during proton therapy using spot scanning. *Int. J. Radiat. Oncol. Biol. Phys.* **53** (1), 244–251.
- STRICKLAND, D. & MOUROU, G. 1985 Compression of amplified chirped optical pulses. *Opt. Commun.* **56** (3), 219–221.
- TADAMURA, E., KUDOH, T., MOTOOKA, M., INUBUSHI, M., SHIRAKAWA, S., HATTORI, N., OKADA, T., MATSUDA, T., KOSHIJI, T. & NISHIMURA, K. ET AL. 1999 Assessment of regional and global left ventricular function by reinjection Tl-201 and rest Tc-99m sestamibi ECG-gated SPECT: Comparison with three-dimensional magnetic resonance imaging. *J. Am. Coll. Cardiol.* **33** (4), 991–997.
- TANAKA, K. A., SPOHR, K. M., BALABANSKI, D. L., BALASCUTA, S., CAPPONI, L., CERNAIANU, M. O., CUCIUC, M., CUCOANES, A., DANCUS, I. & DHAL, A. ET AL. 2020 Current status and highlights of the ELI-NP research program. *Matter Radiat. at Extremes* **5** (2), 024402.
- VLACHOUDIS, V. 2009 FLAIR: a powerful but user friendly graphical interface for FLUKA. In *Proc. Int. Conf. on Mathematics, Computational Methods & Reactor Physics (M&C 2009)*, Saratoga Springs, New York, , vol. 176.
- VORONIN, A. A. AND ZHELTIKOV, A. M. AND DITMIRE, T. AND RUS, B. AND KORN, G. 2013 Subexawatt few-cycle lightwave generation via multipetawatt pulse compression. *Opt. Commun.* **291**, 299–303.
- VRANIC, M., GRISMAYER, T., FONSECA, R. A. & SILVA, L. O. 2016 Electron-positron cascades in multiple-laser optical traps. *Plasma Phys. Control. Fusion* **59** (1), 014040.
- VSHIVKOV, V. A., NAUMOVA, N. M., PEGORARO, F. & BULANOV, S. V. 1998 Nonlinear electrodynamics of the interaction of ultra-intense laser pulses with a thin foil. *Phys. Plasmas* **5** (7), 2727–2741.
- WANG, P. X., HO, Y. K., YUAN, X. Q., KONG, Q., CAO, N., SESSLER, A. M., ESAREY, E.

- & NISHIDA, Y. 2001 Vacuum electron acceleration by an intense laser. *Appl. Phys. Lett.* **78** (15), 2253–2255.
- WANG, X. B., HU, G. Y., ZHANG, Z. M., GU, Y. Q., ZHAO, B., ZUO, Y. & ZHENG, J. 2020 Gamma-ray generation from ultraintense laser-irradiated solid targets with preplasma. *High Power Laser Sci. Eng.* **8**, e34.
- WEST, D. 1982 In *Ternary Equilibrium Diagrams*. Springer.
- WHEELER, J. A. & LAMB JR, W.E. 1939 Influence of atomic electrons on radiation and pair production. *Phys. Rev.* **55** (9), 858.
- YOUNIS, A. H., DAVIDSON, A., HAFIZI, B. & GORDON, D. F. 2021 Diagnostic Techniques for Particle-in-Cell Simulations of Laser-produced Gamma-rays in the Strong-field QED Regime, arXiv: 2106.16227.
- ZHANG, L. Q., WU, S. D., HUANG, H. R., LAN, H. Y., LIU, W. Y., WU, Y. C., YANG, Y., ZHAO, Z. Q., ZHU, C. H. & LUO, W. 2021 Brilliant attosecond γ -ray emission and high-yield positron production from intense laser-irradiated nano-micro array. *Phys. Plasmas* **28** (2), 023110.
- ZHIDKOV, A., KOGA, J., SASAKI, A. & UESAKA, M. 2002 Radiation Damping Effects on the Interaction of Ultraintense Laser Pulses with an Overdense Plasma. *Phys. Rev. Lett.* **88**, 185002.